



# Metastable Helium Absorptions with 3D Hydrodynamics and Self-consistent Photochemistry. II. WASP-107b, Stellar Wind, Radiation Pressure, and Shear Instability

Lile Wang<sup>1</sup>  and Fei Dai<sup>2</sup> <sup>1</sup>Center for Computational Astrophysics, Flatiron Institute, New York, NY 10010, USA; [lwang@flatironinstitute.org](mailto:lwang@flatironinstitute.org)<sup>2</sup>Division of Geological and Planetary Sciences, California Institute of Technology, Pasadena, CA 91125, USA

Received 2020 December 18; revised 2021 March 21; accepted 2021 March 24; published 2021 June 21

## Abstract

This paper presents simulations of the metastable helium ( $\text{He}^*$ ) observations of WASP-107b, so far the highest signal-to-noise ratio detection that is confirmed by three different instruments. We employ full 3D hydrodynamics coupled with coevolving nonequilibrium thermochemistry and ray-tracing radiation, predicting mass-loss rates, temperature profiles, and synthetic  $\text{He}^*$  line profiles and light curves from first principles. We find that a stellar wind stronger than solar is demanded by the observed heavily blueshifted line profile and asymmetric transit light curve. Radiation pressure can be important for  $\text{Ly}\alpha$  observations, but *not*  $\text{He}^*$ . Our model finds that WASP-107b is losing mass at a rate of  $\dot{M} \simeq 1.0 \times 10^{-9} M_{\oplus} \text{ yr}^{-1}$ . Although  $\dot{M}$  varies by  $<1\%$  given constant wind and irradiation from the host, shear instabilities still emerge from wind impacts, producing  $\sim 10\%$  fluctuations of  $\text{He}^*$  transit depths over hour-long timescales. The common assumption that  $\text{He}^*$  transit depth indicates the fluctuation of  $\dot{M}$  is problematic. The trailing tail is more susceptible than planet adjacency to the shear instabilities; thus, the line profile is more variable in the blueshifted wing, while the transit light curve is more variable after midtransit. We stress that the synergy between  $\text{Ly}\alpha$  (higher altitudes, lower density) and  $\text{He}^*$  (lower altitudes, higher density) transit observations, particularly simultaneous ones, yields better understanding of planetary outflows and stellar wind properties.

*Unified Astronomy Thesaurus concepts:* [Exoplanet atmospheres \(487\)](#); [Exoplanet evolution \(491\)](#); [Exoplanet astronomy \(486\)](#); [Astrochemistry \(75\)](#); [Hydrodynamical simulations \(767\)](#); [Astronomical simulations \(1857\)](#); [Hydrodynamics \(1963\)](#)

## 1. Introduction

The “He I  $\lambda 10830$  line” or the “metastable helium line” ( $\text{He}^*$  line for short) transitions between the  $2^3S$  and the upper  $2^3P_J$  ( $J = 0, 1, 2$ ) states are radiatively decoupled from the ground state (for a magnetic dipole transition) and have slow spontaneous decay rates:  $A \simeq 1.3 \times 10^{-3} \text{ s}^{-1}$  (Drake 1971). The high cosmic abundance of helium, the absence of interstellar absorption, and the observability from the ground together enable the  $\text{He}^*$  lines as a unique probe of atmospheric outflows from exoplanets. The first secure detection of  $\text{He}^*$  in transmission was made for WASP-107b with the Hubble Space Telescope (HST; Spake et al. 2018). This detection rekindled decade-long interest in this transition (Seager & Sasselov 2000; Turner et al. 2016; Oklopčić & Hirata 2018); many more detections around other exoplanets have been made since then (e.g., Allart et al. 2018; Nortmann et al. 2018; Salz et al. 2018; Kirk et al. 2020; Ninan et al. 2020).

There is no surprise that WASP-107b was the first exoplanet to show  $\text{He}^*$  detection. The host is young and active ( $\sim 600$  Myr from gyrochronology; chromospheric activity index  $S = 0.89$ ; see also Dai & Winn 2017), expected to give out strong high-energy radiation that powers planetary photoevaporative outflow. The host’s spectral type is K6, which is right at the sweet spot of the EUV–far-UV (FUV) flux ratio that maximally favors the  $\text{He}^*$  absorption (Oklopčić 2019; Wang & F. Dai 2021, hereafter Paper I). The planet is puffy and susceptible to outflows: it has a mass of an icy giant ( $0.12 M_{\text{Jup}}$ ) but a radius closer to that of Jupiter ( $0.94 M_{\text{Jup}}$ ). The optical transit depth is  $\sim 2.2\%$ , while the  $\text{He}^*$  transit depth is a whopping  $\sim 7\%$ . The mean density of the planet is only  $\sim 0.19 \text{ g cm}^{-3}$ , which is reminiscent of the anomalously low-density planets “super-puffs” (e.g., Chachan et al. 2020; Libby-Roberts et al. 2020). Wang & Dai (2019) and

Gao & Zhang (2020) proposed that “super-puffs” may appear inflated owing to high-altitude dusts or hazes elevated by an outflowing atmosphere; the near-infrared HST observation (Kreidberg et al. 2018) is indeed suggestive of high-altitude condensates partially muting the transmission features. WASP-107b is also dynamically interesting. Dai & Winn (2017) suspected that the planet is on a polar orbit owing to the lack of repeating spot-crossing events. More recently, a Rossiter–McLaughlin measurement by Rubenzahl et al. (2021) confirmed this suspicion and thus demands a dynamically hot formation and evolution pathway that may involve the nontransiting planet 107c ( $P \sim 1100$  days,  $M \sin i \sim 110 M_{\oplus}$ ; C. Piaulet et al. 2021).

These reasons render WASP-107b a unique and interesting system. The  $\text{He}^*$  transits of WASP-107b have been observed multiple times (Allart et al. 2018; Spake et al. 2018; Kirk et al. 2020). Its well-resolved line profile exhibits asymmetric shape skewing toward the blueshifted wing, which suggests a comet-like tail. The line ratio of three different  $2^3P_J$  levels also seems to deviate from the simple quantum degeneracy ratio of 1:3:5 (or 1:8 given that the last two are not distinguishable). Having been confirmed by different instruments (CARMENES; Keck/NIRSPEC), these features are likely attributed to the morphology and kinematics of planetary outflows, rather than instrumental effects.

The  $\text{He}^*$  data set of WASP-107b is potentially very revealing and should be analyzed in detail. Two models have been presented in the literature: the 1D isothermal model by Oklopčić & Hirata (2018) assumes the density and velocity profile of a Parker wind (Parker 1958). The model has to assume, rather than predict, the mass-loss rate and temperature of the outflow. Moreover, 1D models are unable to capture the full orbital dynamics and cannot produce a comet-like tail. The

alternative model is the EVaporating Exoplanets code (EVE; see Bourrier et al. 2015; Allart et al. 2018). The lower layer (thermosphere) of this model is also a Parker wind solution; the upper layer is a Monte Carlo particle simulation with He particles under the influence of planetary and stellar gravity and radiation pressure. As we will elaborate later in this work, nevertheless, a particle-based code may not be appropriate for simulating He\* transits. The authors of EVE acknowledged that the particle-based treatment of radiation pressure accelerates the outflow way too quickly: they had to artificially decrease the stellar spectrum near the He\* lines by a factor of  $\sim 50$  to achieve reasonable agreement with the observations of WASP-107b. Shaikhislamov et al. (2021) and Khodachenko et al. (2021) further improved the details of transmission spectra modeling for the hot Jupiter GJ3470b, as well as WASP-107b, based on the incorporation of the photochemical processes of hydrogen and helium in 3D hydrodynamic simulations (see also Khodachenko et al. 2015; Shaikhislamov et al. 2018). These works feature consistent multidimensional multifluid hydrodynamics, yet the coevolved photochemistry has a simplified one-band high-energy radiation model and a size-limited thermochemical network. Impacts of such simplifications are subtle but deterministic, which we will also discuss later in this paper.

In this work, we apply to WASP-107b our model that conducts 3D hydrodynamics, self-consistent thermochemistry, ray-tracing radiative transfer, and especially the processes that populate and destroy He\* (see the first paper in the series, Paper I). Starting from the observed stellar and planetary properties, and making assumptions of the high-energy spectral energy distribution (SED) of the host, we can predict the mass-loss rate, the temperature profile, the ionization states, and the various He\* simulations of WASP-107b. We will also use WASP-107b as a case study to investigate how stellar wind, radiation pressure, and shear instability affect planetary outflows and their observability.

This paper is structured as follows: In Section 2, we briefly describe our model and simulation setup. In Section 3, we present the fiducial model of WASP-107b, which shows remarkable agreement with observations. In Section 4, we perturb the fiducial model in various parameters to investigate the impact of different physical parameters. Section 6 summarizes the paper and suggests prospective improvements for the future.

## 2. Methods

### 2.1. Basic Setup

Our numerical simulation suite was described in detail in Paper I, based on the framework combining thermochemistry, hydrodynamics, and radiation, described in Wang & Dai (2018, hereafter WD18). For a brief recap, we analytically set up a self-gravitating model for the planet interiors using the equations of state tabulated by Miguel et al. (2016), so that the planet mass  $M_p$  and the effective optical transiting radius  $\langle r_{\text{eff}} \rangle$  both match the observed data. The simulations are conducted on 3D spherical polar meshes, whose origin resides on the planet center, and the polar axis points to the host star. They have the gravitation of both the host star and the planet, as well as the effects of orbital motion including centrifugal and Coriolis forces. Our code computes ray-tracing radiative transfer and nonequilibrium thermochemistry simultaneously

with hydrodynamics. For simplicity, we assume a circular orbit and that the planet is tidally locked, adopting a corotating planet-centric frame. We focus on the upper layer of the atmosphere, including a quasi-isothermal layer assumed to have equilibrium temperature and an outflowing region irradiated by high-energy photons. To guarantee that all relevant optical and thermochemical phenomena take place inside the simulation domain, we set the inner radial boundary of our spherical polar mesh slightly below  $\langle r_{\text{eff}} \rangle$ . The hydrodynamic boundary conditions there are set according to the readily calculated model of planet interiors.

We describe the high-energy SED of the host star with six representative energy bins:

1. 2 eV for the near-infrared, optical, and near-ultraviolet bands ( $1 \mu\text{m} \geq \lambda > 2500 \text{ \AA}$ ).
2. 7 eV for FUV photons ( $2500 \text{ \AA} \geq \lambda > 1100 \text{ \AA}$ ; “soft FUV”); note that these photons can ionize He\*.
3. 12 eV for the Lyman–Werner (“LW”) band FUV photons that photodissociate molecular hydrogen ( $1100 \text{ \AA} \geq \lambda > 912 \text{ \AA}$ ).
4. 20 eV for “soft EUV” photons that ionize hydrogen but not helium ( $912 \text{ \AA} \geq \lambda > 504 \text{ \AA}$ ).
5. 40 eV for EUV and soft X-ray (“hard EUV”) photons that ionize helium ( $504 \text{ \AA} \geq \lambda > 50 \text{ \AA}$ ).
6. 3 keV photons for the X-ray ( $\lambda \leq 50 \text{ \AA}$ ).

We make synthetic observations including He\* line profiles and transit light curves in the vicinity of the He\* line. To further facilitate comparisons between observation and simulations, we compute summary statistics such as the equivalent widths  $\langle W_\lambda \rangle \equiv \int \Delta\epsilon(\lambda) d\lambda$ , the radial velocity shift of the absorption peak  $\Delta v_{\text{peak}}$ , and the FWHM of the absorption-line profile.

Specifically for WASP-107, Anderson et al. (2017) reported a K6 host star with a mass of  $M_* = 0.69 M_\odot$ , a radius of  $R_* = 0.66 R_\odot$ , and an effective temperature of  $T_{*,\text{eff}} = 4430 \text{ K}$ . Planet b orbits its host on a near-circular but polar orbit (Dai & Winn 2017, C. Piaulet et al. 2021; Rubenzahl et al. 2021). The semimajor axis is  $a = 0.055 \text{ au}$  where the equilibrium temperature is  $T_{\text{eq}} = 740 \text{ K}$ ; the transit light curve indicates a small impact parameter ( $b = 0.07$  Dai & Winn 2017). WASP-107b has an optical transiting radius of  $R_p \simeq 0.94 R_{\text{Jup}}$  and a mass  $M_p \simeq 0.12 M_{\text{Jup}}$ .

### 2.2. Including Stellar Wind and Radiation Pressure

The He\* observables of WASP-107b are highly suggestive of an outflow morphology similar to a comet-like tail, as the reader will find out shortly (Sections 3.1, 3.2). We explore two possible mechanisms that may give rise to the comet-like tail: stellar wind and radiation pressure. For stellar winds, although realistic patterns of stellar winds could be very complicated, we take a very basic approach here. The stellar wind is injected as a hydrodynamic flow in a simulation, with two velocity components in the planet frame: (1) a radial component centered at the host star, and (2) a headwind due to orbital motion of the planet. The first component has the radial wind speed as a parameter; the second one is set to be equivalent to the orbital velocity of the planet.

The regions of interactions between the stellar wind and the planet outflow are illustrated by Figure 1. Depending on whether the velocity already becomes supersonic before being decelerated and deflected by the impinging stellar wind, a fluid element in the planet outflow should go through the sonic

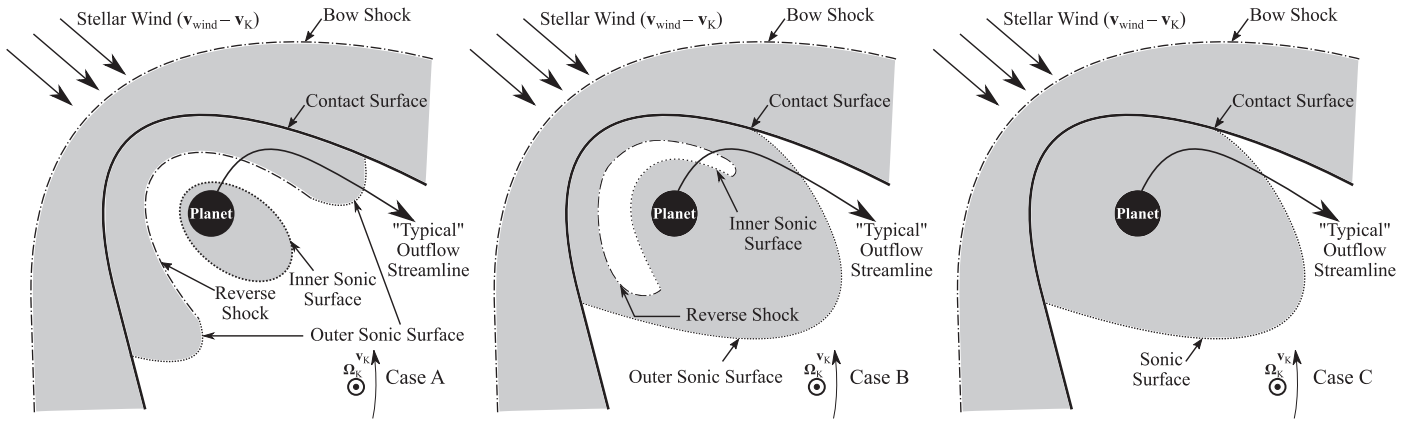


**Figure 1.** Schematic diagrams (not to scale) of the interactions between a stellar wind and a planetary atmospheric outflow (see also Section 2.2). In all panels, the host star resides to the left of the diagrams, and the planet’s linear Keplerian velocity points upward within the paper plane (see the indicators of  $v_K$  and  $\Omega_K$  in the lower left corner of all panels). Subsonic regions are illustrated by gray shades. Typical streamlines are indicated by thin solid lines with arrow heads. Shock fronts, including the bow shocks and the reverse shock, are indicated by dashed–dotted lines. Contact surfaces (contact discontinuities) are shown by thick solid lines. Dotted lines indicate the sonic critical surfaces. The left panel, marked as Case A, shows a typical case that part of the planet outflow experiences initial thermally driven acceleration, reverse shock deceleration (due to the stagnation and deflection by the stellar wind), and final acceleration by expansion. Note that the outer sonic surface is connected to the reverse shock, and any streamline crossing the outer sonic surface *must* go through the reverse shock front. The middle panel presents Case B, which is qualitatively similar to Case A but has different topologies owing to a relatively weaker planetary outflow. The right panel presents another typical Case C with a weaker planetary wind, which does not have a reverse shock: the planet outflow stays subsonic before the stagnation and deflection and only becomes supersonic after it already escapes from the “trap” shaped by the stellar wind.

critical surface twice (part of the streamlines in “Case A” and “Case B”) or once (the complement part of streamlines in Cases A and B, and all streamlines in “Case C”). Different cases represent different relative strengths of the planetary outflows compared to the stellar winds. Case A stands for the situation where the planetary outflow has a considerably higher total pressure compared to the impinging stellar wind. Case C stands on the opposite side of Case A, where the planet blows a wind with much weaker total pressure than the star, and the contact surface does not need a reverse shock to deflect the subsonic part of the planet wind. The intermediate Case B stands in between. We note that a streamline in Cases A and B *must* go through the reverse shock when and only when it crosses the sonic critical surface twice. The first sound crossing occurs at smaller radii (“inner” sonic surface) as the fluid element is accelerated by the thermal pressure gradient. However, as the upwind part is impinged by the stellar wind, the streamline travels through a reverse shock and is decelerated to subsonic. The fluid element then changes its direction and becomes deflected to move onto the nightside. The confinement due to stellar wind then becomes weaker, and the fluid element is allowed to expand like in a de Laval nozzle before eventually becoming supersonic again at a second (“outer”) sonic surface. Other streamlines go through the inner sonic surface only and never touch the outer sonic surface or the reverse shock front.

The planetary outflow may also have chemical interactions with the impinging stellar wind. As was pointed out by, e.g., Holmström et al. (2008), Tremblin & Chiang (2013), Bourrier et al. (2013, 2016), Bourrier & Lecavelier des Etangs (2013), and Ehrenreich et al. (2015), the charge exchange between the stellar wind protons ( $H^+$ ) and planet-origin neutral hydrogen (H) may produce a considerable abundance of nonthermal neutral hydrogen atoms. We nonetheless note, for the situations within this paper, that the mean free path (MFP) of charge and momentum exchange during the collision between stellar and planetary winds is usually tiny compared to the hydrodynamic

length scales. Since sufficient momentum exchange leads to thermalization, we find that the hydrodynamic mixture between the planet and stellar wind materials is a good first-order representation that includes the outcome of charge exchange (see also Christie et al. 2016; McCann et al. 2019). The other charge exchange processes between neutral and ionized atoms and molecules (24 reactions in total) are readily included in the thermochemical network (see McElroy et al. 2013).

Stellar winds impose more stringent Courant–Friedrichs–Lewy conditions: each model takes  $\sim 51$  hr to run on a 40-core, four-GPU computing node of the Popeye-Simons Computing Cluster. To accelerate the convergence of our simulations, in addition to the “adaptive coarsening” technique in Paper I, we also adopt a two-step scheme of simulation: (1) turn on hydrodynamics, thermochemistry, and radiative transfer and run the simulation for  $\sim 15 \tau_{\text{dyn}}$  until the model almost reaches the quasi-steady state without stellar winds; and (2) turn on the stellar wind and continue the simulation for  $\gtrsim 200 \tau_{\text{dyn}}$  until the final quasi-steady state is reached. The dynamical timescale for a  $T \sim 10^4$  K photoevaporative outflow around WASP-107b is estimated as  $\tau_{\text{dyn}} \sim 4.8 \times 10^3$  s:

$$\tau_{\text{dyn}} \sim \frac{GM_p}{c_s^3} \sim 1.2 \times 10^3 \text{ s} \times \left( \frac{M_p}{10 M_{\oplus}} \right) \left( \frac{T}{10^4 \text{ K}} \right)^{-3/2}. \quad (1)$$

To ensure that the simulations are not limited by the spatial resolution of the simulation grid, we ran a model with a higher resolution ( $N_{\log r} \times N_{\theta} \times N_{\phi} = 192 \times 192 \times 128$ ), and the results are almost identical to that of our standard grid.

Another potentially influential factor is the radiation pressure. We added this effect to our ray-tracing radiative transfer procedures by explicitly computing the momenta deposited by the photons absorbed or scattered. For each photon energy bin  $h\nu$  (Section 2.1), during each time step  $\Delta t$ , the momentum density variation caused by radiation for a mesh

cell reads

$$\Delta \mathbf{p}(h\nu) = \sum_r \left( \frac{h\nu}{c} \right) \frac{\delta N_{\text{ph},r}(h\nu)}{\Delta V} \hat{n}_r, \quad (2)$$

where the summation index “ $r$ ” runs through all rays that go through the current cell,  $\Delta V$  is the volume of the cell,  $\delta N_{\text{ph},r}(h\nu)$  is the number of  $h\nu$  photons deduced from the  $r$ th ray within this cell, and  $\hat{n}_r$  is the unitary direction vector of the ray. We note that  $\delta N_{\text{ph},r}(h\nu)$  is calculated by considering the local number of photons held by the ray, the proper geometry, and the opacity given by all absorption and scattering processes (including photochemistry) for the photon energy bin  $h\nu$  based on the current abundances of chemical species for the particular cell (see [WD18](#) and references therein). Note also that each ray subtends a small solid angle, and the photon number per ray per unit time is integrated over  $\Delta t$ , so that the units and normalization are not confused in Equation (2). By summing up the momentum increments caused by all  $h\nu$  energy bins, the momentum density variation (vector) and energy variation (scalar) are both updated for the hydrodynamic solver as source terms. Equivalently, the radiation causes an acceleration in that cell,

$$\mathbf{a} = \sum_{h\nu,r} \left( \frac{h\nu}{c} \right) \frac{\delta N_{\text{ph},r}(h\nu)}{\rho \Delta V \Delta t} \hat{n}_r, \quad (3)$$

where  $\rho$  stands for the total mass density in the cell, and the summation of  $h\nu$  runs through all energy bins. Self-shielding and cross-shielding effects for each relevant photon energy bin, which could affect both the chemistry and the radiation pressure, have been taken into account by the recipes summarized in [Draine & Bertoldi \(1996\)](#) and [Heays et al. \(2017\)](#). Note that the photon energy bins that are most responsible for  $\text{Ly}\alpha$  and  $\text{He}^*$  absorption acceleration are *not* included in the fiducial model. Nonetheless, as Section 5.1 will discuss, after adding the two photon energy bins for  $\text{Ly}\alpha$  and  $\text{He}^*$  to the model specifically, the radiative pressure caused by these two absorption lines still plays a minor role in the overall dynamics and  $\text{He}^*$  observables.

### 3. WASP-107b: An Outflow Shaped by Stellar Winds

#### 3.1. Observation Results

Quantitatively, we directly compare our synthetic observations to  $\text{He}^*$  line profiles and light curves. The  $\text{He}^*$  transmission spectrum of WASP-107b is both spectrally and temporally resolved with different spectrographs: NIRSPEC and CARMENES ([Spake et al. 2018](#); [Allart et al. 2019](#); [Kirk et al. 2020](#)). We also carried out an independent analysis of the transit observed from NIRSPEC on the Keck telescope on 2019 April 6 (same as [Kirk et al. 2020](#)). Our data reduction is carried out using the procedures described in [Zhang et al. \(2021\)](#).  $\text{He}^*$  transits have been observed by several different instruments and different transit events. Despite the differences in instrumental characteristics and reduction pipelines, previous  $\text{He}^*$  observations agree with each other on the following features: (1) a non-Keplerian, blueshifted ( $\sim 2\text{--}3 \text{ km s}^{-1}$ ) line profile; (2) a line ratio that deviates from the 1:3:5 (viz., the quantum degeneracies; apparently 1:8) among three  $\text{He}^*$  transitions; and (3) elongated ingress and egress timescales in

$\text{He}^*$  transit light curves. Finally, in the temporally resolved observation ([Kirk et al. 2020](#)), there is a hint of asymmetry in the outflow morphology that the egress lasts longer than the ingress while the egress is more blueshifted compared to the midtransit.

#### 3.2. Fiducial Model Setup and Necessity of Stellar Winds

As noted in Paper I, consistent 3D hydrodynamic simulations with all physics are not sufficiently fast for a comprehensive exploration of the parameter space using Markov Chain Monte Carlo or even just gradient descent. Instead, we adopt the parameters based on the reported stellar and planetary conditions. The optical and near-infrared fluxes (represented by the  $h\nu = 2 \text{ eV}$  bin) simply accord with the host star radius and effective temperature. The high-energy SED of the host star is much more uncertain. Guided by the results in our Paper I, i.e., how various high-energy radiation bins affect the atmospheric outflow and  $\text{He}^*$  observables, we hand-tuned independently within a plausible range for each individual parameter: (1) the high-energy SED (especially in the FUV, soft EUV, and hard EUV bins), and (2) stellar wind radial velocity and density (the tangential velocity component is invariant), until reasonable agreement with the observations is reached. The resulting high-energy SED for the fiducial model (see Table 1) is fairly typical or slightly more active than a K5 star ([Gudel 1992](#); [France et al. 2016](#); [Loyd et al. 2016](#); [Youngblood et al. 2016, 2017](#); [Oklopčić 2019](#)). The stellar wind parameters, compared to the Sun ([Venzmer & Bothmer 2018](#)), have a rather ordinary radial velocity at such a close distance ( $270 \text{ km s}^{-1}$  at 0.055 au), while the density is higher ( $\sim 10^5 m_p \text{ cm}^{-3}$ ), resulting in a relatively strong stellar wind (stellar mass-loss rate  $\sim 6 \times 10^{-13} M_\odot \text{ yr}^{-1}$ ). Nevertheless, we also note that WASP-107b has a relatively short rotation period of 17 days, and the  $\sim 600 \text{ Myr}$  host star has a strong chromospheric  $S$  index (0.89) ([Dai & Winn 2017](#)); therefore, higher UV luminosities and stronger winds can be expected.

In addition to tuning the high-energy SED, we found it crucial to include stellar wind components in our simulations to adequately reproduce the existing  $\text{He}^*$  observations. We first run a series of no-wind models as we did in Paper I for WASP-69b with different fluxes in each energy bin. The resultant outflow is always largely spherically isotropic, without a prominent comet-like tail. In a test model that has no wind and is otherwise equivalent to the fiducial model, the overall equivalent width of the line profile is weaker ( $\langle W_\lambda \rangle \simeq 7.6 \pm 0.2 \text{ \AA}$  in the fiducial model, but  $\langle W_\lambda \rangle \simeq 5.0 \text{ \AA}$  in the no-wind model). More importantly, the line profile does not have a stronger blueshifted wing, which has been validated by several different instruments. The impinging stellar wind stagnates the outflow flowing toward the host star (i.e., the redshifted wing), pushing the outflow to the nightside (the blueshifted wing). The transit light curve in the no-wind model is also much more symmetric owing to the lack of comet-like tail trailing behind the planet. Qualitatively speaking, that the spectral and temporal asymmetries indicate star-centered repelling force has already been concluded by a few theoretical and observational studies about the  $\text{Ly}\alpha$  profiles of planetary outflows (e.g., [Bourrier et al. 2015, 2016](#); [Lavie et al. 2017](#); [McCann et al. 2019](#); [Debrecht et al. 2020](#)). In short, a no-wind model struggles, if ever possible, to reproduce the various  $\text{He}^*$  observations of WASP-107b. On the other hand, the windy

**Table 1**  
Properties of the Fiducial Model for WASP-107b

Item	Value
Simulation domain	
Radial range	$10.21 R_{\oplus} \leq r \leq 400 R_{\oplus}$
Latitudinal range	$0 \leq \theta \leq \pi$
Azimuthal range	$0 \leq \phi \leq \pi$
Resolution ( $N_{\log r} \times N_{\theta} \times N_{\phi}$ )	$144 \times 128 \times 64$
Planet interior <sup>a</sup>	
$M_{\text{rcb}}$	$38.1 M_{\oplus}$
$\langle r_{\text{eff}} \rangle$	$10.6 R_{\oplus}$
Radiation flux (photons $\text{cm}^{-2} \text{s}^{-1}$ )	See Section 3.2
2 eV (IR/optical)	$2.1 \times 10^{19}$
7 eV (soft FUV)	$1.2 \times 10^{16}$
12 eV (LW)	$3 \times 10^{12}$
20 eV (soft EUV)	$2 \times 10^{13}$
40 eV (hard EUV)	$6 \times 10^{13}$
3 keV (X-ray)	$2 \times 10^{12}$
Initial abundances [ $n_X/n_H$ ]	Same as Paper I
H <sub>2</sub>	0.5
He	0.1
H <sub>2</sub> O	$1.8 \times 10^{-4}$
CO	$1.4 \times 10^{-4}$
S	$2.8 \times 10^{-5}$
Si	$1.7 \times 10^{-6}$
Gr	$1.0 \times 10^{-7}$
Dust/PAH properties	Same as Paper I
$\sigma_{\text{dust}}/H$ (effective specific cross section)	$8 \times 10^{-22} \text{ cm}^2$
Stellar wind (at $a = 0.055 \text{ au}$ )	See Section 3.2
Density	$1.7 \times 10^{-19} \text{ g cm}^{-3}$
Temperature	$10^6 \text{ K}$
Radial velocity	$270 \text{ km s}^{-3}$
Tangential velocity <sup>b</sup>	$106 \text{ km s}^{-3}$
Abundances <sup>c,d</sup> [ $n_X/n_H$ ]	
e <sup>-</sup>	$\simeq 1.1^e$
H <sup>+</sup>	1.0
He <sup>+</sup>	0.1
O <sup>+</sup>	$3.2 \times 10^{-4}$
C <sup>+</sup>	$1.4 \times 10^{-4}$
S <sup>+</sup>	$2.8 \times 10^{-5}$
Si <sup>+</sup>	$1.7 \times 10^{-6}$

**Note.**

<sup>a</sup> Mass and transit radius of the planet core; see also Appendix A of Paper I for details of planet core setups.

<sup>b</sup> Headwind component; same as the Keplerian velocity.

<sup>c</sup> Because the wind injection has a star-centered geometry, these values are calibrated at the planetary orbit, viz.,  $a = 0.055 \text{ au}$ .

<sup>d</sup> Calibrated at the domain boundary of wind injection.

<sup>e</sup> Electrical neutrality is guaranteed.

model successfully reproduced observed He\* line profiles and light curves. We now examine the windy model in detail.

### 3.3. Fiducial Model Results

Figure 2 presents the simulation results of our fiducial model, with a stellar wind modulating the outflow morphology. Each panel is centered at the planet’s frame; the host star is located to the left of the plot, and the stellar wind impinges on the photoevaporative outflow at an angle given by the ratio between the radial velocity component and the headwind (orbital) component. A bow shock of Mach number  $\sim 2.0$  forms above the dayside of the planet, heating the downstream flow to  $T \sim 4 \times 10^6 \text{ K}$  (second panel of Figure 2). As shown by the

streamlines, the photoevaporative outflow from the planet is stalled at the dayside and directed by stellar wind to the nightside, forming a prominent tail trailing the planet’s orbital motion. It is easily estimated that, near the envelope of the tail (i.e., the contact surface), the MFP of proton–neutral hydrogen collision is at the order of  $\sim 10^{-1} R_{\oplus}$ . Such MFPs are tiny compared to the hydrodynamic length scales, confirming the legitimacy of our approximation on charge exchange in Section 2.2.

Along the thick streamline in Figure 2 (which qualitatively resembles the “typical” streamline in Figure 1), we plot the spatial variation of key hydrodynamic and thermochemical quantities as a function of both the radius from the planet core and the arc length along the streamline in Figure 3. Looking at the outflow velocity first, a fluid element traveling on the streamline may experience multiple sound crossings, as is shown by the Case B in Figure 1 (see also Section 2.2). The bottom panel of Figure 3 indicates that the population of He\* is determined primarily by the equilibrium between recombination excitation and collisional de-excitation at smaller radii. At larger radii ( $\gtrsim 10^2 R_{\oplus}$ ), photoionization by soft FUV photons starts to take over. This is very similar to our results in Paper I for WASP-69b.

The middle panel of Figure 3 shows another interesting feature. When the streamline crosses the the planet’s shadow, photoionization due to soft FUV from the host star vanishes. Meanwhile, recombination excitation continues in the shadow of the planet and thus creates a local bump of higher He\* abundances. We call this effect the “shadow tail”—such a “two-tail” morphology is remarkably similar to the dust and ion tails of comets, although with different underlying physics. The shadow tail is difficult to observe in transits, as it always hides in the planet’s shadow. Once the bulk of the outflow has highly suppressed abundances of He\* (e.g., by excessive FUV fluxes from an A-type or F-type host star; see also Paper I; Oklopčić 2019), however, the tail will become the biggest reservoir of He\* in the system. In this case, if one is ever able to resolve this photoevaporative outflow, one may see the shadow tail emitting more strongly in He\* compared to other parts of the outflow. As an order-of-magnitude estimation, the luminosity in the 10830 Å lines emitted by the tail with spatial volume  $V_{\text{tail}}$  is roughly

$$\begin{aligned}
 L_{\text{tail}} &\sim V_{\text{tail}} \langle n(\text{He}^*) n_e \rangle k_{10830} \left( \frac{hc}{\lambda} \right) \\
 &\sim 10^{-14} L_{\odot} \times \left( \frac{V_{\text{tail}}}{10^4 R_{\oplus}^3} \right) \\
 &\quad \times \left[ \frac{\langle n(\text{He}^*) n_e \rangle}{10^8 \text{ cm}^{-6}} \right] \left( \frac{k_{10830}}{10^{-7} \text{ cm}^3 \text{ s}^{-1}} \right), \quad (4)
 \end{aligned}$$

where we get the typical values by extrapolating the fiducial model and adopt the  $2^3S \rightarrow 2^3P$  collisional excitation rate  $k_{10830}$  at  $T = 7000 \text{ K}$  (the typical temperature for the densest part of the tail; see Figure 2) from Berrington et al. (1985). Compared to the typical luminosity of an F star at the He\* lines ( $\lesssim 10^{-4} L_{\odot}$  over a 1 Å window assuming  $T_{\text{eff}} = 7000 \text{ K}$ ), the contrast is  $\sim 10^{-10}$ . In the case in which such situations occur at larger angular separation in some other planetary systems hosted by an F star, the tails would be potentially observable by the direct imaging apparatus proposed for the future (Traub & Oppenheimer 2010; Chauvin 2018).

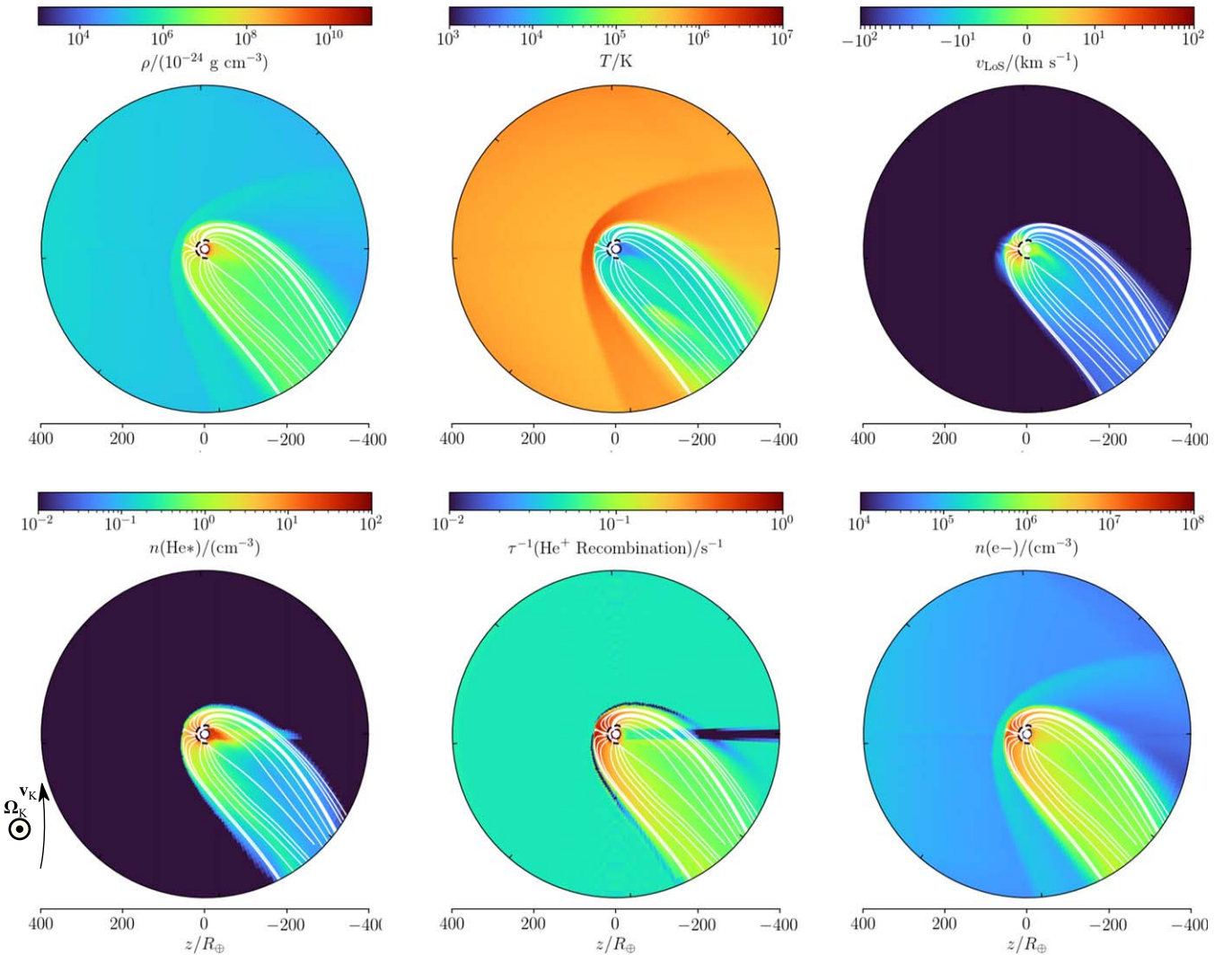


**Figure 2.** Key hydrodynamics and chemistry profiles of the simulation for WASP-107b (fiducial model 107-0) in the quasi-steady-state, averaged through the last  $15 \tau_{\text{dyn}}$ . Stellar radiation comes from the left of the plot, and the orbital angular velocity  $\Omega_K$  points out of the paper plane; the Keplerian motion of the planet is upward  $v_K$ . White streamlines are separated at the *wind base* by  $\Delta\theta = \pi/16$ . Note that only the inner sonic surface is shown (dashed black curve; see also Case B in Figure 1). The heavy streamlines are the reference lines on which the profiles are plotted in Figure 3.

Figure 4 offers a transverse view of the outflow, taken from the perspective of an observer looking into the host star (shown with the white dashed line) during a transit. The planet is moving toward the right-hand side and is instantaneously close to the center of the host star. These plots illustrate the spatial distribution of extinction at three characteristic wavelengths of the He\* transition. At the bluer wavelength  $\lambda = 10832.5 \text{ \AA}$ , which falls into the “valley” between the  $J = 0$  transition and two blended  $J = 1, 2$  transitions, the extinction is dominated by blueshifted materials in the tail trailing behind the planet. On the red wing  $\lambda = 10833.7 \text{ \AA}$ , the tail is much less relevant, and the extinction is generated by materials much closer to the planet. Again, this is attributed to the kinematics and morphology: the planetary outflow is impinged by the stellar wind, and the outflow on the dayside or the headwind direction is stagnated.

Finally, we remind the reader that, due to its large aperture, Keck/NIRSPEC is able to resolve the He\* both spectrally and temporally. Figure 5 compares the observed spectral profiles and light curves (Section 3.1) with the simulated results, in which the fiducial model exhibits remarkable consistency. In even greater detail, Figure 6 presents the observed and

simulated variation of He\* absorption in time and wavelength space together as a heatmap. The vertical dotted lines are the rest-frame wavelengths of three He\* transitions, and the horizontal dashed lines are the expected  $t_1$  to  $t_{1V}$  (starts/ends of the ingress/egress) of the planet’s transit. Our simulation with stellar winds successfully reproduces the key feature: since most of the He\* is produced by the comet-like tail trailing the planet (Figure 4), the strongest absorption occurs after midtransit, while the pre-ingress absorption is much weaker than the post-egress one. This feature is also manifested by the asymmetry in the transit light curve (Figure 5). The outflow morphology loses spherical symmetry; the part ahead of the planet and that behind the planet are both blueshifted. As a result, the He\* line profiles seen pre-ingress and post-egress are both more blueshifted compared to the midtransit line profile. This is again consistent with the NIRSPEC observation.

#### 4. Parametric Studies

The previous section elaborates the fiducial model for WASP-107b. We found that, by including stellar winds, the

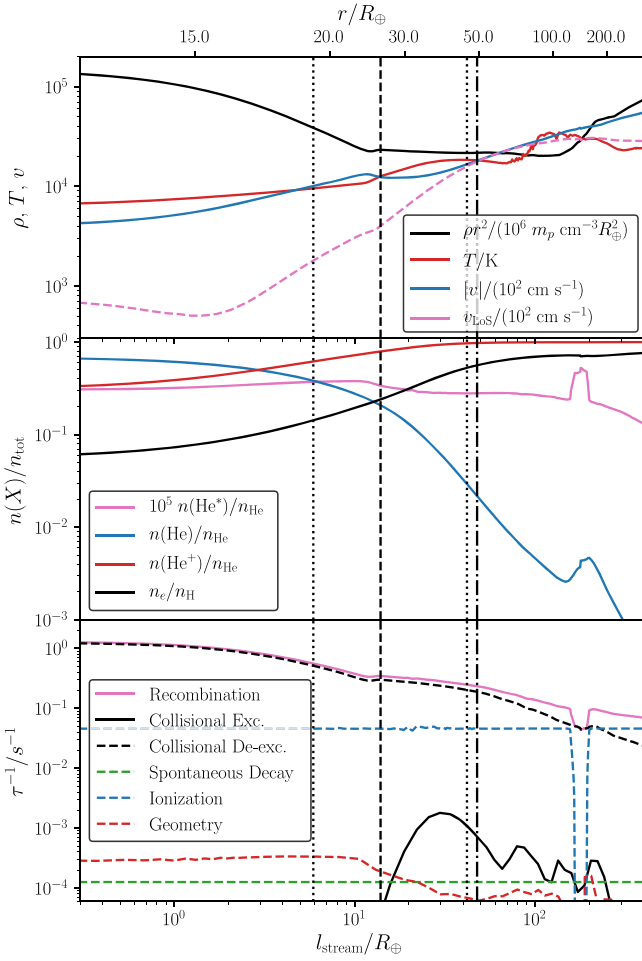


**Figure 3.** Key quantities of our fiducial model for WASP-107b (model 107-0), time-averaged over the last  $15 \tau_{\text{dyn}}$ , along the reference streamlines (plotted as the heavy streamline in Figure 2). The top abscissa is the radial coordinate  $r$  corresponding to the curve length along the streamline on the bottom abscissa. As explained by Section 2.2 and Case B in Figure 1, the fluid elements along this streamline experience two smooth crossings of sonic speed (indicated by vertical dotted lines; note that the right of them is close to the dashed-dotted line for the Roche radius) and a reverse shock (indicated by vertical dashed lines) along the streamline.

simulation quantitatively reproduces various observed features of the  $\text{He}^*$  transits. This section investigates how the outflow morphology and  $\text{He}^*$  observables are affected by each model parameter (Figures 7 and 8). We set a series of models, each differing from the fiducial model by one parameter only unless specifically indicated. Table 2 and Figure 8 summarize the models and their corresponding key  $\text{He}^*$  observables.

#### 4.1. High-energy Radiation Fluxes

Paper I found that  $\text{He}^*$  transit observations are primarily determined by soft FUV (which destroys the  $\text{He}^*$  state) and the EUV bands (which is most important in driving the photoevaporative outflow; interested readers are referred to Paper I for more details); the LW and X-ray bands play secondary roles. We found very similar results for WASP-107b after including stellar winds, by running a separate test simulation excluding X-ray photons (not presented in this paper) that yields almost identical morphology and observables to the fiducial one. In models 107-1 through 107-3, we raise

stellar fluxes in the soft FUV ( $h\nu = 7 \text{ eV}$ ), soft EUV (20 eV), and hard EUV (40 eV) bands, respectively.

Model 107-1 increases the soft FUV flux by a factor of 10. As we have noted earlier, soft FUV does not inject significant heat into the atmosphere and has minor effects in driving the planetary outflow. Its mass-loss rate is very similar to that in the fiducial model [ $(\dot{M}/10^{-9} M_{\oplus} \text{ yr}^{-1}) = 1.08 \text{ vs. } 1.02$ ]. Soft FUV is nonetheless capable of photoionizing the  $\text{He}^*$  state efficiently, slicing the equivalent widths by a factor of 2 ( $(\langle W_{\lambda} \rangle / 10^{-2} \text{ \AA}) = 3.7 \text{ vs. } 7.6$ ). Models 107-2 and 107-3 raise the soft and hard EUV flux level by a factor of 10, respectively. As expected, intense EUV fluxes boosted the photoevaporation rates, indicated by the stronger mass-loss rate and equivalent width. What is curious, however, is that in model 107-3 the planetary outflow is so strong that it pushes back the bow shock with stellar wind on the dayside to much higher altitudes. In order to fully contain the pushed-back contact surface and the bow shock, we use  $r_{\text{out}} = 800 R_{\oplus}$  for the outer radial boundary of model 107-3.<sup>3</sup> This effect is so strong that we begin to see the dayside (pre-ingress) material in redshift, and the overall  $\text{He}^*$  line profile is now biased toward the red wing (Figure 8, top panel). This strong dayside outflow also manifests as a reversed asymmetry in the  $\text{He}^*$  light curve, where the ingress is more extended and stronger than the egress (Figure 8, bottom panel). This qualitative change in behavior will possibly constrain the balance of high-energy radiation strengths between the stellar wind and the planetary outflow.

#### 4.2. How Stellar Winds Shape Outflows

In hydrodynamic simulations (no magnetic effects included), the interactions between stellar winds and planetary outflows should be determined by the wind ram pressure ( $\sim \rho_{\text{wind}} v_{\text{wind}}^2$ ), as a function of the density ( $\rho_{\text{wind}}$ ) and velocity ( $v_{\text{wind}}$ ). Fortunately, this degeneracy between wind density and velocity can be potentially broken by orbital motion, i.e., the headwind component of the stellar wind.

On one hand, model 107-4 quadruples the density  $\rho_{\text{wind}}$  and halves the velocity  $v_{\text{wind}}$ , thus keeping the radial (from host to planet) component of ram pressure roughly the same as in the fiducial model. The headwind component, caused by the Keplerian motion  $v_{\text{K}}$  of the planet, is held constant here. Lower velocity shear yields a less turbulent trailing tail with weaker shear instabilities. As a result, the tail lags behind the planet in both velocity and spatial sense, producing a more blueshifted line profile ( $(\Delta v_{\text{peak}} / \text{km s}^{-1}) = -4.5$ , vs.  $-3.5$  for the fiducial) and a more asymmetric light curve. On the other hand, in model 107-5, which doubles the velocity but quarters the density, the tail is now influenced by the radial component more heavily. It is primarily directed toward the nightside and displays considerably more vigorous shear instabilities owing to greater velocity shears. The  $\text{He}^*$  light curve has much weaker post-egress absorption, while the equivalent width sees more variability ( $(\langle W_{\lambda} \rangle / 10^{-3} \text{ \AA}) = 7.4 \pm 0.4$ , versus  $7.6 \pm 0.2$  in the fiducial model). Finally, model 107-6 only increases the density  $\rho_{\text{wind}}$  by a factor of two. Having the same ratio of  $v_{\text{wind}}/v_{\text{K}}$  as in the fiducial model, model 107-6 produces a tail that has similar direction to the fiducial model. Increased ram

<sup>3</sup> We carried out another simulation run that has  $r_{\text{out}} = 400 R_{\oplus}$  (same as other runs) for the radial boundary, while all other physical conditions remain the same as model 107-3. It is confirmed that this test run (not shown in the paper) has all quantitative characteristics almost identical to 107-3, despite that its mass-loss rate is  $\sim 5\%$  greater.

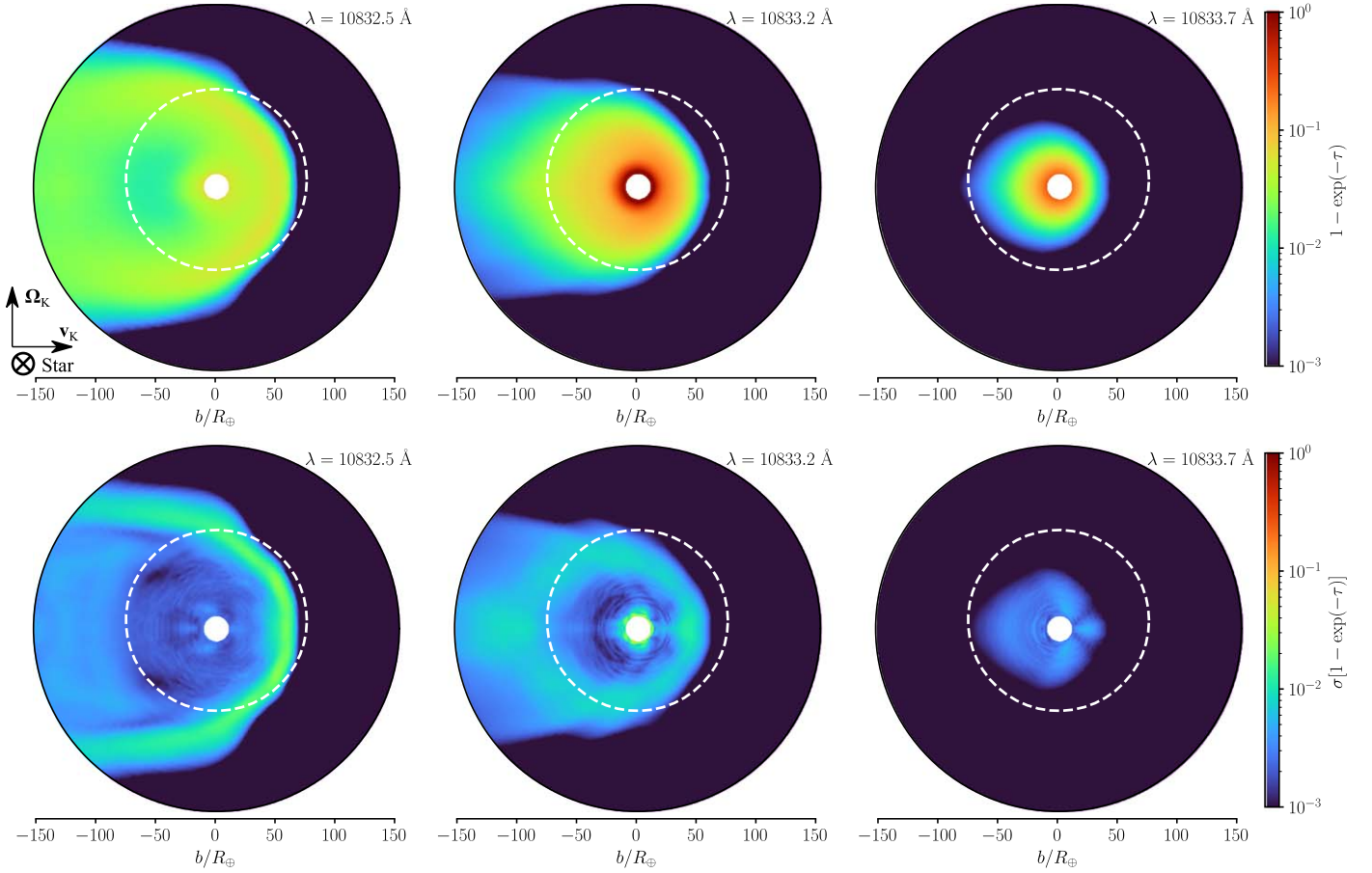


**Figure 4.** First row: extinction  $[1 - \exp(-\tau)]$  for model 107-0 with time-averaging over the last  $\sim 15 \tau_{\text{dyn}}$  (note that the averaging is computed *after* the extinction function is calculated for *each* snapshot concerned) at three representative wavelengths  $(\lambda/\text{\AA}) \in \{10832.5, 10833.2, 10833.7\}$  near the  $\text{He}^*$  transitions. The profiles are measured at midtransit. The second row presents the rms variations of extinction  $(\sigma[1 - \exp(-\tau)])$ , plotted up to the impact parameter  $b = 150 R_{\oplus}$ . The white dashed circles presenting the host star size have  $R_* \simeq 74.2 R_{\oplus}$  and orbit impact parameter  $b \simeq 0.07 R_*$ .

pressure still pushes the outflow to greater blueshift velocities ( $(\Delta v_{\text{peak}}/\text{km s}^{-1}) = -5.6$  vs.  $-3.5$ ).

## 5. Discussions

### 5.1. Tail: Stellar Wind or Radiation Pressure?

As we have shown in the previous sections, the existing  $\text{He}^*$  observations of WASP-107b are suggestive of a comet-like tail that trails the photoevaporating planet. What is the mechanism that gives rise to these tails? Is it stellar wind, or radiation pressure, or a combination of these two effects? When studying the  $\text{Ly}\alpha$  outflow for exoplanets, previous studies often attributed transit asymmetry to radiation pressure (e.g., GJ 436b; Bourrier et al. 2015, 2016). Some other studies, using different numerical simulation paradigms, contended that the  $\text{Ly}\alpha$  radiation pressure is insignificant (e.g., Khodachenko et al. 2019 for GJ 436b; Khodachenko et al. 2017; Debrecht et al. 2020 for HD 209458b), or may have comparable impacts as stellar winds (Esquivel et al. 2019; Villarreal D’Angelo et al. 2021). A few recent works on  $\text{He}^*$  followed suit on the radiation pressure side: in the EVE simulations of WASP-107b (collisionless particle-based simulations; Allart et al. 2018, 2019), the authors found that their prescription of radiation pressure accelerates the outflow way too quickly, producing a tail that is directly pointing away from the nightside of the planet. Their prescribed effect of radiation pressure is so strong that the authors had to artificially decrease the stellar spectrum near the  $\text{He}^*$  lines by a factor of 50

to achieve reasonable agreement with the observations of WASP-107b. We argue, in this work, (1) that particle-based simulations are not adequate to account for the effect of radiation pressure on  $\text{He}^*$  transitions, and (2) that the completeness of photochemistry is crucial in reaching the consistent conclusion about the radiation pressure on  $\text{He}^*$ .

We must first clearly distinguish the  $\text{Ly}\alpha$  transition and the  $\text{He}^*$  transitions. The lower state of  $\text{Ly}\alpha$  is the ground state of neutral hydrogen, while  $\text{He}^*$  (i.e., the  $2^3S$  state of helium) is relatively much more difficult to populate and has much lower abundances throughout the domain of interest ( $\lesssim 10^{-5}$ ; Figure 3; see also Paper I; Oklopčić 2019). Meanwhile, the product of the Einstein  $A$ -coefficient and the overall element abundance for helium is also  $\sim 10^2$  times smaller than  $\text{Ly}\alpha$ . Consequently, the altitude where most  $\text{He}^*$  absorption occurs is often much lower than the  $\text{Ly}\alpha$  absorption region. The gas density in these regions is significantly higher, and the MFP of momentum transfer is much shorter. In our simulations, we typically see  $n(\text{H}^+) \gtrsim 10^6 \text{ cm}^{-3}$  and an MFP of  $\lambda = 1/[n(\text{H}^+)\sigma] \lesssim 10^3 \text{ cm}$  (see also Thomas & Humberston 1972; Draine 2011). This is  $\sim 6$  orders of magnitude smaller than the hydrodynamic length scales. Such a contrast in length scales demands a hydrodynamic treatment, instead of a collisionless particle-based one. What is more, the momenta deposited into  $\text{He}^*$  by absorption are quickly diluted and thermalized by more collisions. In contrast, a collisionless particle-based treatment such as EVE is more appropriate for simulating the  $\text{Ly}\alpha$  outflow, since the density where most

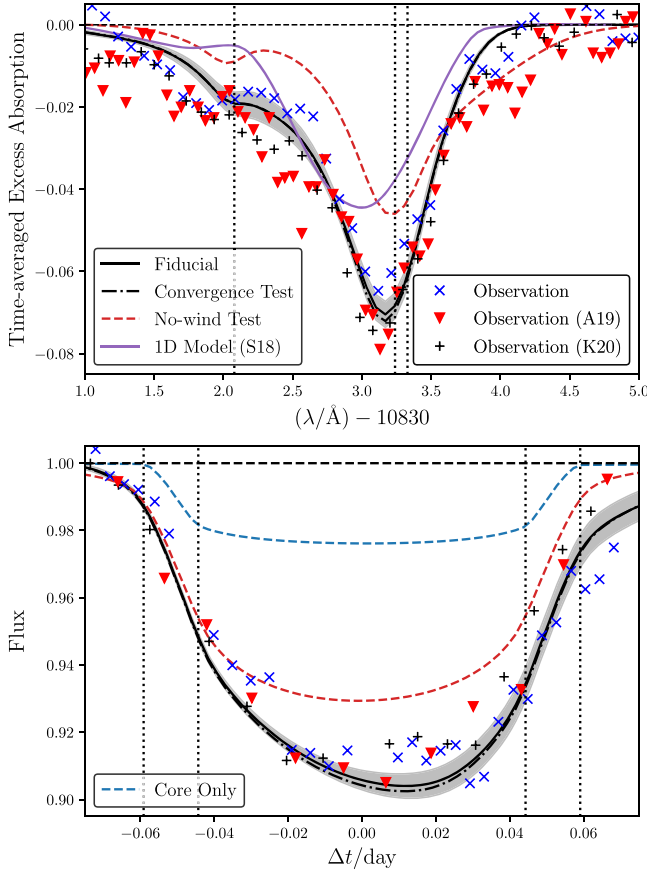


**Figure 5.** Observed and synthesized line profiles and light curves for the fiducial model of WASP-107b and its corresponding test models. Curves for all models indicate the averages of the spectral profile and light curves over the last  $15 \tau_{\text{dyn}}$  (note that they are obtained by calculating the profiles for each snapshot *before* taking the average, *not* by evaluating the profiles for the time-averaged model). Gray shades around the curves for the fiducial model in both panels express the range of two times standard deviation ( $2\sigma$ ) over the last  $15 \tau_{\text{dyn}}$ . The observation results in Kirk et al. (2020) are denoted by black plus signs and labeled with “Observation (K20)”; those marked with red triangles and “Observation (A19)” present the results in Allart et al. (2019). Although the error bars of observation data are omitted for clearer plots, we note that the agreement of the fiducial model with observations is within the error bars. The 1D spherical symmetric model in Spake et al. (2018) is included for reference, marked by the magenta curve with label “1D Model (S18)” in the top panel. For reasonable comparisons, the window function for light curves is taken to be the same as Kirk et al. (2020), i.e., a top-hat function that has unitary value in  $(\lambda/\text{\AA}) \in [10833.05, 10833.48]$  and zero elsewhere (note that the window in Allart et al. 2019 is different,  $(\lambda/\text{\AA}) \in [10832.80, 10833.55]$ ). Vertical dotted lines in the top panel show the centers of the three  $\text{He}^*$  lines and mark the start/end of the nominal ingress/egress ( $t_1$  through  $t_4$ ) in the bottom panel.

$\text{Ly}\alpha$  absorption occurs is much lower: in our no-wind test simulation, we have  $n(\text{H}^+) \lesssim 10^{-1} \text{cm}^{-3}$  and the MFP is  $\lambda \sim 10^{10} \text{cm} \sim 10 R_{\oplus}$ . Neutral hydrogen atoms there are essentially decoupled from other components of the gas and are indeed susceptible to the momentum deposited by the absorption of  $\text{Ly}\alpha$ . It is worth noting that, in some specific situations where the  $\text{Ly}\alpha$  absorption takes place at higher density, hydrodynamic simulations are also required for modeling  $\text{Ly}\alpha$  radiation pressure properly (see, e.g., Esquivel et al. 2019; Debrecht et al. 2020, and the comparisons to Bourrier et al. 2013 therein). We hence summarize that the requirement on numerical tools is situation dependent for  $\text{Ly}\alpha$ , while for  $\text{He}^*$  hydrodynamic methods are essential.

The consistency of photochemistry is emphasized by the comparison with Khodachenko et al. (2021), which ranked the

radiation pressure above stellar winds in shaping the tail for WASP-107b. The underlying reason for the difference is that their calculations included only one representative energy bin for EUV and X-ray (XUV). The FUV photons, which have been confirmed as the predominant destructor of  $\text{He}^*$  in the outer regions (Figure 3; see also Paper I; Oklopčić 2019), were neglected. The inefficiency of XUV in destroying  $\text{He}^*$ , because of much weaker fluxes (see Table 1; Section 2.1) and reduced cross sections (Norcross 1971) compared to the FUV, allows a significant amount of  $\text{He}^*$  atoms to survive at very high altitudes ( $r \gtrsim 20 R_p \sim 200 R_{\oplus}$ ; see Figure 1 in Khodachenko et al. 2021), where the gas is attenuated and the radiation pressure indeed matters. However, there are two important facts to notice. First, a K-type host star has a considerable power in the FUV radiation, which is improper to ignore (Table 1; see also Oklopčić 2019; Paper I). Second, such an extended  $\text{He}^*$  absorption region would result in a  $\gtrsim 0.25$ -day length of transits on the helium lines, which is at odds with the observation data (Figures 5 and 6).

We set up a verification test simulation to numerically examine the effect of radiation pressure. Two more photon energy bins are added to the ray-tracing radiative transfer module: one has  $h\nu = 10.2 \text{ eV}$  ( $\lambda = 1216 \text{ \AA}$ ) for  $\text{Ly}\alpha$ , and one has  $h\nu = 1.15 \text{ eV}$  ( $\lambda = 10833 \text{ \AA}$ ) for the metastable helium lines. The luminosities are taken to be typical for K-type stars: we adopt  $L_{1.15 \text{ eV}} \simeq 10^{-5} L_{\odot}$  (assuming a  $T = 4400 \text{ K}$  black-body spectrum and a  $1 \text{ \AA}$  effective width) and also  $L_{\text{Ly}\alpha} \simeq 10^{-5} L_{\odot}$  (see Wood et al. 2005). For these two energy bins *only*, we assume for simplicity that the cross sections for photon momentum absorption are equal to the line-center values. We also ignore (1) the self-shielding effect and (2) the dispersion process of  $\text{Ly}\alpha$  photons in the frequency space caused by reemission for these two bins. We note that these simplifications should only amplify the effects of radiation pressure. Under these assumptions, the ratio of radiation pressure acceleration by the helium lines  $a_{\text{He}^*}$  to the local gravitational acceleration by the planet  $g_p$  roughly reads

$$\begin{aligned} \frac{a_{\text{He}^*}}{g_p} &\sim \frac{n(\text{He}^*)}{n_{\text{H}}} \left[ \frac{F(1.15 \text{ eV}) \sigma(\text{He}^*)(h\nu/c)}{GM_p m_p / r^2} \right] \\ &< 10^{-4} \times \left[ \frac{n(\text{He}^*)/n_{\text{He}}}{10^{-5}} \right] \left( \frac{L_{1.15 \text{ eV}}}{10^{-5} L_{\odot}} \right) \\ &\times \left( \frac{a}{0.05 \text{ au}} \right)^{-2} \left( \frac{M_p}{40 M_{\oplus}} \right)^{-1} \left( \frac{r}{10 R_{\oplus}} \right)^2, \end{aligned} \quad (5)$$

where  $r$  is the distance to the planet center and the inequality sign arises from ignoring the extinction. Note that, after the inequality sign, we have replaced the dilution factor  $[n(\text{He}^*)/n_{\text{H}}]$  with  $[n(\text{He}^*)/n_{\text{He}}]$  for easier comparisons ( $n_{\text{H}}$  and  $n_{\text{He}}$  stand for the total nucleus number density of hydrogen and helium, respectively). For  $\text{Ly}\alpha$ , the estimation is similar, but the radiation acceleration should be compared to the stellar gravity ( $g_* \equiv GM_*/a^2$ ), since the region of absorption usually resides near or outside the Roche radius,

$$\begin{aligned} \frac{a_{\text{Ly}\alpha}}{g_*} &\sim \frac{n(\text{H})}{n_{\text{H}}} \left[ \frac{F_{\text{Ly}\alpha} \sigma_{\text{Ly}\alpha} (h\nu/c)}{GM_* m_p / a^2} \right] \\ &< 0.3 \times \left[ \frac{n(\text{H})/n_{\text{H}}}{10^{-2}} \right] \left( \frac{L_{\text{Ly}\alpha}}{10^{-5} L_{\odot}} \right) \left( \frac{M_*}{M_{\odot}} \right). \end{aligned} \quad (6)$$

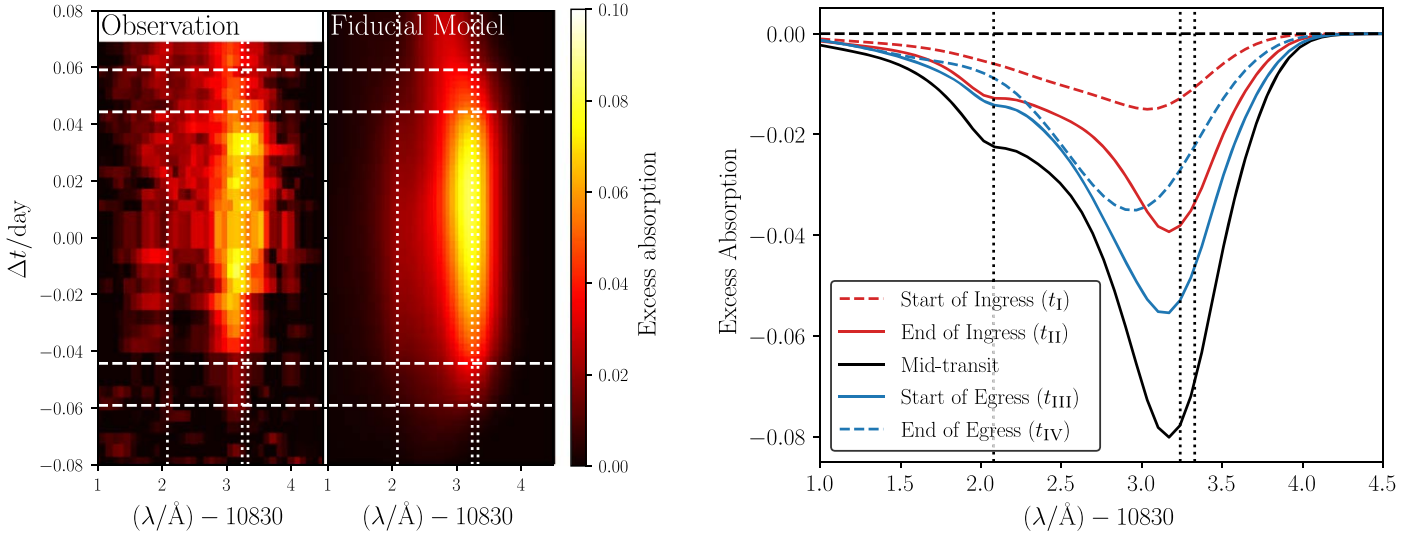


**Figure 6.** Left panel: comparison of the excess absorption features, as functions of transit time  $\Delta t$  and wavelength  $\lambda$ , between the observation data (left panel) and the synthesized results (right panel). The simulation used to produce the right panel is the time-averaged fiducial model 107-0 (averaging is taken in the same way as in Figure 5, viz., averaging *after* the excess absorption map being obtained for each snapshot concerned). Both panels already have the wavelength shifts by orbital motion subtracted (viz., in the planet frame). Three vertical dotted lines in each panel indicate the line centers. Four horizontal dashed lines indicate the starts (ends) of the ingress (egress). Right panel: transmission spectra at different stages of a transit, based on the fiducial model 107-0.

**Table 2**  
Results of Various Models, Based on the Fiducial Model for WASP-107b

Model	Description	$\dot{M}$ ( $10^{-9} M_{\oplus} \text{ yr}^{-1}$ )	$\langle W_3 \rangle$ ( $10^{-2} \text{ \AA}$ )	$\Delta v_{\text{peak}}$ ( $\text{km s}^{-1}$ )	FWHM ( $\text{km s}^{-1}$ )
107-0	Fiducial	$1.02 \pm 0.01$	$7.6 \pm 0.2$	-3.5	22.7
107-1	$10 \times \text{Flux at } h\nu = 7 \text{ eV}$	$1.09 \pm 0.01$	$3.7 \pm 0.1$	-1.7	17.2
107-2	$10 \times \text{Flux at } h\nu = 20 \text{ eV}$	$1.23 \pm 0.01$	$11.3 \pm 0.9$	-3.7	34.6
107-3	$10 \times \text{Flux at } h\nu = 40 \text{ eV}$	$3.47 \pm 0.03$	$12.1 \pm 1.1$	2.4	55.1
107-4	$4 \times \rho_{\text{wind}}, 1/2 \times v_{\text{wind}}$	$0.98 \pm 0.02$	$8.6 \pm 0.1$	-4.5	20.4
107-5	$1/4 \times \rho_{\text{wind}}, 2 \times v_{\text{wind}}$	$1.02 \pm 0.01$	$7.4 \pm 0.4$	-2.3	22.6
107-6	$2 \times \rho_{\text{wind}}$	$0.99 \pm 0.02$	$8.2 \pm 0.1$	-5.6	28.2

**Note.** The values and errors are time averages and three times the standard deviations ( $3\sigma$ ), respectively; the time averages are taken over the last  $25 \tau_{\text{dyn}}$  of the simulations.

It is obvious that, with ordinary stellar luminosity near the  $\text{He}^*$  lines, radiation acceleration by these lines should always be negligible. On the other hand, a higher luminosity in  $\text{Ly}\alpha$  is possible to repel neutral hydrogen atoms away from the star efficiently.

We confirm that the test simulation produces almost identical results to the fiducial model in terms of hydrodynamic and thermochemical profiles, as well as  $\text{He}^*$  observables. In addition, Figure 9 compares the magnitudes of acceleration (force per unit mass) by radiation pressure (where most  $\text{He}^*$  absorption occurs), gas pressure gradient, and inertial force (including stellar and planetary gravitation, centrifugal force, and Coriolis force) for this test model along the radial line pointing to the star. Radiation acceleration in this model is more than one order of magnitude weaker than the hydrodynamic effects, even at the  $r \sim 40 R_{\oplus}$  “spike,” which corresponds to the increased absorption of  $\text{Ly}\alpha$  near the contact surface. We confirm that this comparison is still valid along other radial lines, where the  $\text{Ly}\alpha$  absorption “spikes” are even less prominent near the contact surface. These comparisons are largely consistent with Equations (5) and (6), although one should notice that the hydrodynamic acceleration ( $|\nabla p|/\rho$ ) takes a greater share than

the stellar gravity at the  $\text{Ly}\alpha$  absorption front near the contact surface. Again, the high density of the  $\text{He}^*$  absorbing region maintains sufficiently strong momentum coupling of different species and guarantees quick dilution of the momenta injected by photons. Because of the confinement provided by the stellar wind, for the models we discuss in this paper, even the  $\text{Ly}\alpha$  absorption region becomes sufficiently dense. Therefore, following similar arguments to those for  $\text{He}^*$ , the radiation pressure effects of  $\text{Ly}\alpha$  also have secondary importance.

In summary, at least for  $\text{He}^*$  lines, radiation pressure only plays a minor role in shaping the outflow morphology and kinematics. Stellar wind, as we have shown in the previous section, is essential in reproducing various observed features of  $\text{He}^*$  transitions. We propose that, should future observations of  $\text{He}^*$  show strong deviations from a “quiescent” line ratio ( $\sim 1:8$ ) or an asymmetry in line profile or light curve, it may be regarded as an indication of stellar winds, whose properties can be constrained with detailed 3D hydrodynamic simulations.

### 5.2. Shear Instability

At the contact surface that separates the stellar wind and the photoevaporative outflow, there is a region of large shears in

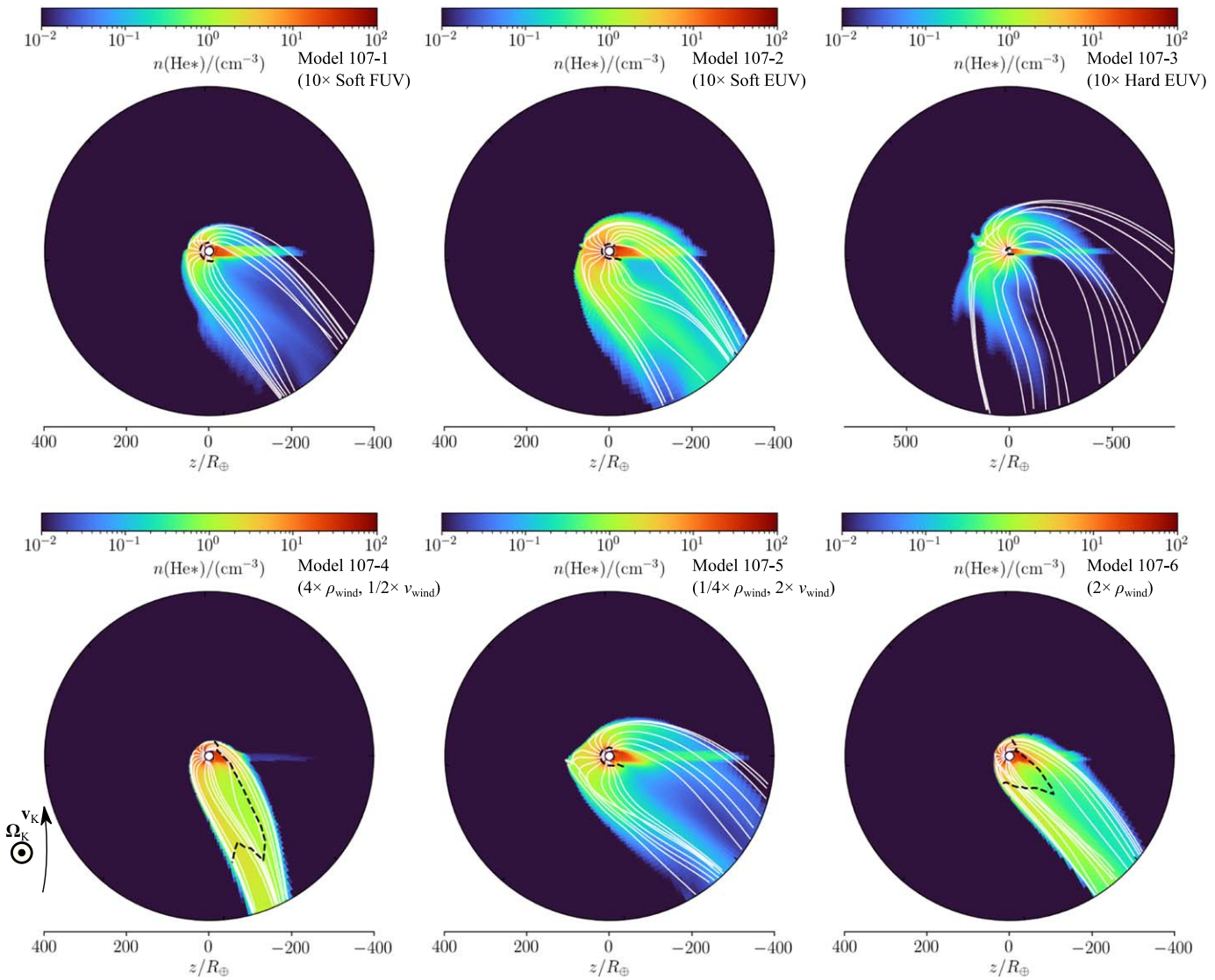


**Figure 7.**  $\text{He}^*$  number density profiles in the orbital plane, with streamlines (spaced with the same scheme as in Figure 2) and sonic surfaces overlaid. The panel for model 107-3 has different spatial scales. Some lines appear to overlap with other lines or to terminate before reaching the outer boundary because the streamlines are projected. Note that models 107-4 and 107-6 comply with Case C in Figure 1.

velocity. Shear instabilities are generated here, manifesting themselves as billowing outflows. We found that since the sonic surface is located at much lower altitude (Figure 1; see also Figure 3), the outflow mass-loss rate is not affected by these shear instabilities. If the host star high-energy SED is held constant, the mass-loss rate stays rather stable ( $<1\%$  fluctuation) at about  $\dot{M} \simeq 1.02 \times 10^{-9} M_{\oplus} \text{ yr}^{-1}$  in our fiducial model of WASP-107b. However, part of the  $\text{He}^*$  absorption takes place at higher altitudes (Figure 4) and is directly influenced by shear instabilities. Fluctuations of transit depths have relative amplitudes of  $\sim 5\%$  to  $\sim 20\%$  at different wavelengths, while the typical timescale is  $\sim 0.2$  days (Figure 10). In contrast, in our WASP-69b model in Paper I, shear instabilities are not excited since stellar wind was not included.  $\text{He}^*$  absorption shows  $\lesssim 0.5\%$  temporal variations. We notice that the charge exchange production of  $\text{He}^*$  at the contact surface is more than two orders of magnitude slower than (i.e.,  $\lesssim 10^{-2}$  times compared to) the recombination with free electrons. Therefore, such fluctuations in  $\text{He}^*$  absorption represent the hydrodynamic

influence on the planet wind by the shear instabilities, instead of the instability billows themselves.

An interesting prediction associated with shear instability is that there should be much stronger fluctuations in the blueshifted wings of  $\text{He}^*$  line profiles. Moreover, in the  $\text{He}^*$  light curve, the variability should be much stronger after the midtransit point. The reason is that shear instability takes time and space to grow: its spatial extent is still small in the redshifted head part of the outflow, but fully developed when it enters the blueshifted tail. In Figure 5, the gray shaded region indicates the amplitudes of variability due to shear billows and clearly demonstrates this fluctuation-induced asymmetry. Up to the composition of this paper, two  $\text{He}^*$  transits have been reported; more transits, preferably from the same instruments, are needed to evaluate the fluctuation asymmetries.

### 5.3. Line Ratio Probes Kinematics Instead of Density

It has been suggested that the line ratios between three transitions of  $\text{He}^*$  can tell us about the density of the underlying

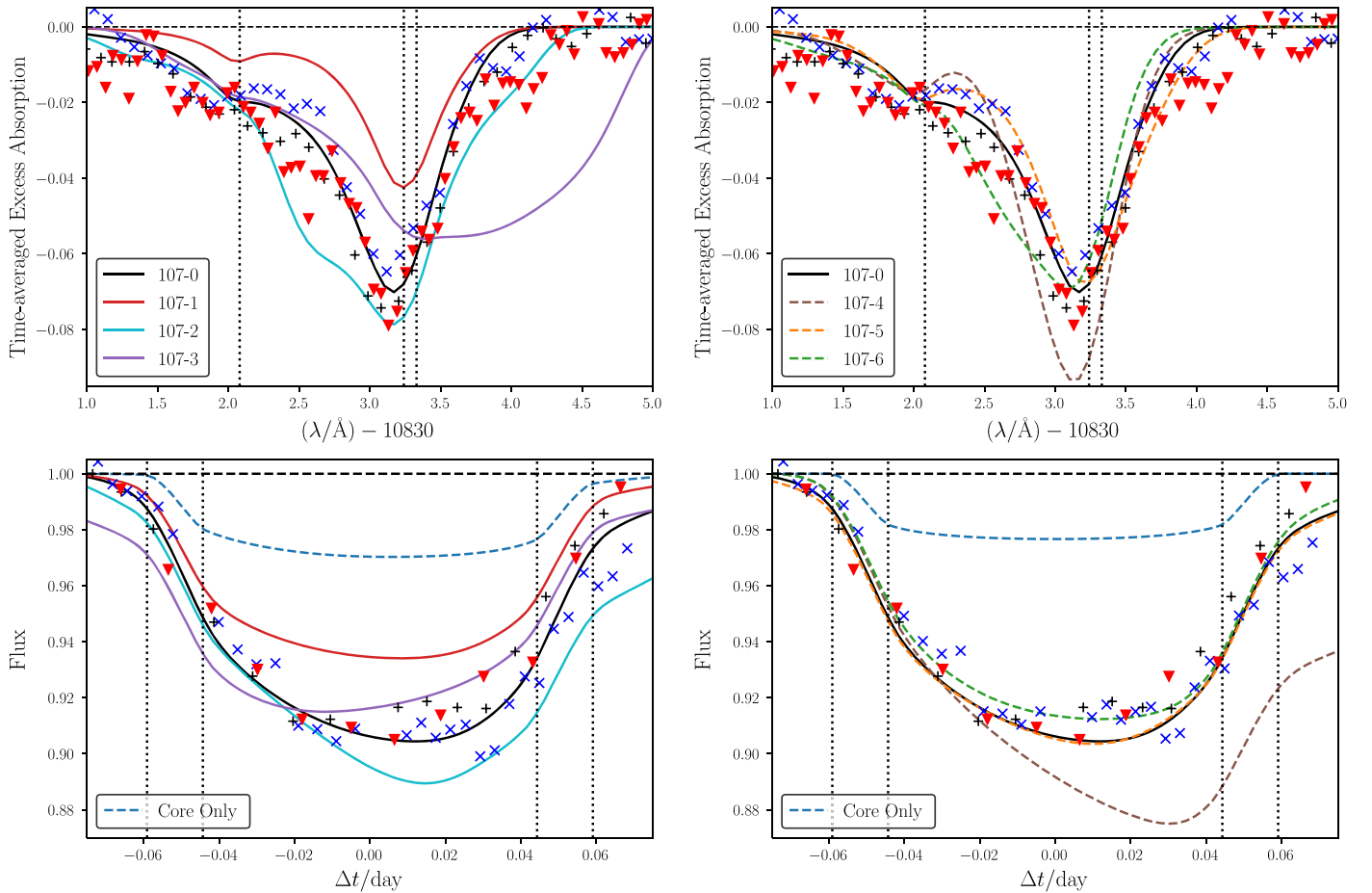


**Figure 8.** Similar to Figure 5, but for the models in Section 4.2 and Table 2. The left column compares models 107-1 through 107-3 to the fiducial 107-0, and the right column does the comparison for models 107-4 through 107-6 to 107-0. The window function for the light curves is the same as the one used to yield Figure 5.

outflow. If all three lines are not saturated, the line ratios between the triplet should be proportional to 1:3:5, or their quantum degeneracies. Considering that the two longer-wavelength transitions are often blended together thermally and kinematically, the line ratio should be 1:8. Now if the density of the outflow is high enough that the transitions start to saturate, the line ratio may begin to deviate from 1:8 and provide hints about the number density of  $\text{He}^*$  in the outflow. However, as we have seen in Paper I for WASP-69b and in this paper for WASP-107b, most of the  $\text{He}^*$  extinction happens at the regions of  $10^1 - 10^2 R_\oplus$  (see Figure 4, showing the midtransit extinction at three characteristic wavelengths near the  $\text{He}^*$  transitions). The lines are far from saturation in these regions. In other words, the line ratios cannot directly probe the density distribution at least for WASP-107b.

We do observe a line ratio of about 1:4 in our fiducial model of WASP-107b, which is significantly different from the 1:8 expected by quantum degeneracies. It is noted that this deviation is primarily caused by the kinematics of the outflow: the peaks due to two longer-wavelength transitions are blueshifted by the wind by up to  $\sim 20\text{--}30 \text{ km s}^{-1}$ , so that its blueshifted wing starts to invade the shorter-wavelength transition. We will see in the next subsection that the line ratio and the exact shape of the  $\text{He}^*$ , given proper information about the high-energy SED of the host star, will serve as a probe of the outflow kinematics and in turn the properties of stellar wind.

Here we present an example that one can semiquantitatively constrain the stellar wind density and velocity using the  $\text{He}^*$  observation. We shall focus on the contact discontinuity, i.e., the boundary separating the stellar wind and the planetary outflow (Figures 1, 2). The distance of contact discontinuity from the planet, without magnetic fields, can be estimated by equating the total pressure of a photoevaporative outflow to the ram pressure of the stellar wind  $\rho_{\text{wind}} v_{\text{wind}}^2$ :

$$\begin{aligned}
 r_{\text{cd}} &\sim \left[ \frac{\dot{M}_s}{\pi \rho_{\text{wind}} v_{\text{wind}}^2} \right]^{1/2} \\
 &\sim 500 R_\oplus \times \left( \frac{\dot{M}}{10^{-9} M_\oplus \text{ yr}^{-1}} \right)^{1/2} \left( \frac{T}{10^4 \text{ K}} \right)^{1/4} \\
 &\quad \times \left( \frac{\rho_{\text{wind}}}{10^{-20} \text{ g cm}^{-3}} \right)^{-1/2} \left( \frac{v_{\text{wind}}}{100 \text{ km s}^{-1}} \right)^{-1}, \quad (7)
 \end{aligned}$$

where the subscript “cd” stands for the contact discontinuity. In our fiducial model, this estimation yields  $r_{\text{cd}} \sim 45 R_\oplus$  with the parameters in Table 1. This is reasonably accurate with visual inspection of Figure 2. We note that if the stellar wind intensity is similar to the Sun at an  $a = 0.055 \text{ au}$  orbit, which roughly has  $\rho_{\text{wind}} \sim 3 \times 10^3 m_p \text{ cm}^{-3}$  and  $v_{\text{wind}} \sim 300 \text{ km s}^{-1}$  at  $\sim 0.05 \text{ au}$  (see Venzmer & Bothmer 2018 and references therein),  $r_{\text{cd}} \sim 240 R_\oplus$  would be inconsistent with the observations of WASP-107b. Such stronger stellar wind experienced by

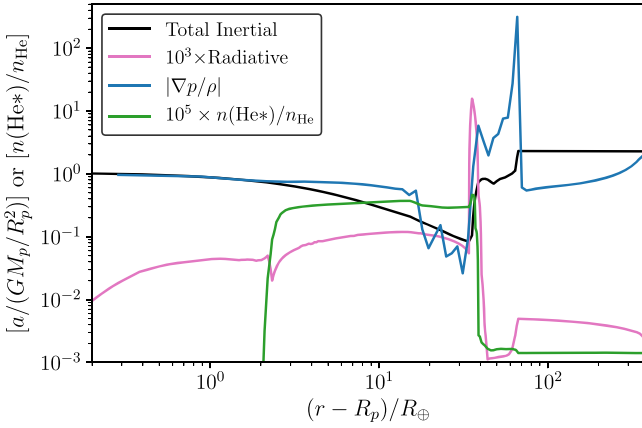


**Figure 9.** Profiles of acceleration magnitudes (normalized by  $GM_p/R_p^2$ ) along the radial line pointing to the host star, plotted for the test simulation that contains extra photon energy bins at  $\text{Ly}\alpha$  and  $10833 \text{ \AA}$  radiated by the host star (Section 5.1). Inertial acceleration (including planet and stellar gravity, centrifugal force, and Coriolis force), radiation pressure acceleration (multiplied by  $10^3$ ), and pressure gradient acceleration profiles are measured along the  $\theta = \pi/4$ ,  $\phi = 0$  radial line. The radiation pressure profile is multiplied by  $10^3$  for clearer presentation. As a reference, the relative abundance of  $\text{He}^*$  (multiplied by  $10^5$ ) is also shown.

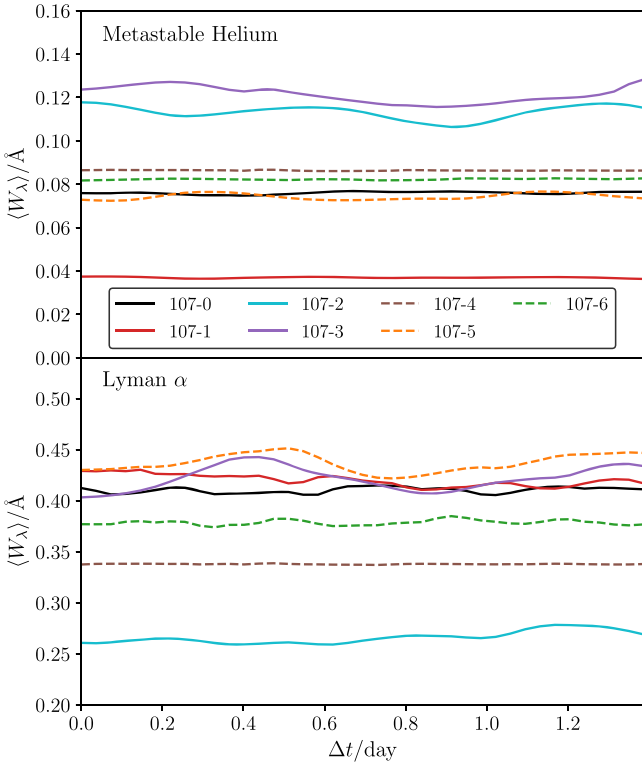


**Figure 10.** Temporal variation of the equivalent widths of the metastable helium absorption lines (top panel) and  $\text{Ly}\alpha$  (bottom panel), for the models described in Table 2. Such fluctuations are mainly the results of the instabilities emerging in the interactions between stellar wind and planetary outflows. For each simulation, the last 1.4 days  $\sim 25 \tau_{\text{dyn}}$  of its simulated time duration are shown.

WASP-107b is perhaps not surprising, given its closer-in orbit and the relative youth and higher activity of the host star.

#### 5.4. Synergy between $\text{Ly}\alpha$ and $\text{He}^*$ Observations

This section briefly discusses how observing transits of an exoplanet in both  $\text{Ly}\alpha$  and  $\text{He}^*$  can be synergistic in helping us

understand its atmospheric outflow. First of all, we reiterate the point made in Section 5.1 that most  $\text{Ly}\alpha$  absorption happens at much higher altitudes than  $\text{He}^*$  absorption. The low density at higher altitude means that  $\text{Ly}\alpha$  radiation pressure may start to reshape the morphology of neutral hydrogen, while at the lower altitude of  $\text{He}^*$  absorption, radiation pressure heats rather than pushes the planetary outflow. This potentially allows us to disentangle the influence of radiation pressure and stellar wind and to disentangle the inner and outer parts of the planet outflow.

We produced synthetic line profiles and light curves in the  $\text{Ly}\alpha$  band for WASP-107b in Figure 12. Note that we did not account for the extinction due to the interstellar medium. We also note that  $\text{Ly}\alpha$  observations are currently unavailable for WASP-107b and will probably remain so given the distant host and the expected strong UV extinction. However, we still notice that the line profile is blueshifted significantly while the  $\text{Ly}\alpha$  light curve shows much more pronounced asymmetry with elongated egress. Both of these observations are qualitatively similar to other exoplanets observed in  $\text{Ly}\alpha$  (e.g., GJ 436b; see also Bourrier et al. 2015, 2016; Ehrenreich et al. 2015). The no-wind model produces deep  $\text{Ly}\alpha$  transit light curves, whose ingress and egress elongated to a similar extent. We also find that, by setting up another no-wind test model using the same simplified radiation pressure model as Section 5.1 (which again overestimates the  $\text{Ly}\alpha$  radiation acceleration), the radiation pressure by  $\text{Ly}\alpha$  alone is not sufficient to produce as strong an asymmetry as in the fiducial model.

Another prediction we can draw from the combination of  $\text{Ly}\alpha$  and  $\text{He}^*$  is that the absorption fluctuations due to shear instabilities tend to be stronger in  $\text{Ly}\alpha$  than in  $\text{He}^*$ . Because of the high relative abundance and absorption efficiency of neutral hydrogen, the lines of sight threading through the shear instability billows, where the density is usually much lower than the inner  $\text{He}^*$  absorption regions, can experience significant absorption and thus represent the hydrodynamic fluctuations in  $\text{Ly}\alpha$  (see Figure 11). In addition, instabilities grow as they propagate from the “bulge” region to the tail, so the fluctuations in  $\text{Ly}\alpha$  should lag behind those in  $\text{He}^*$ . The shaded bands in Figure 12 illustrate the simulated variations in  $\text{Ly}\alpha$  absorption, which is considerably more prominent than their counterparts in  $\text{He}^*$  (Figure 5).

Before the inclusion of the  $\text{He}^*$  lines, there have been various works discussing the  $\text{Ly}\alpha$  detectability of stellar wind and planetary outflow interactions. Tremblin & Chiang (2013) and Christie et al. (2016), using 2D hydrodynamic simulations, argued that the fluctuations of absorption could indicate the variations near the contact surface at relatively high velocities ( $\gtrsim 100 \text{ km s}^{-1}$ ). Esquivel et al. (2019) had similar conclusions in 3D simulations. McCann et al. (2019) carried out 3D simulations focusing on hot Jupiters and concluded that the Coriolis force and stellar winds are indispensable factors in shaping the asymmetry of planetary outflows (for similar conclusions see also Carolan et al. 2020; Shaikhislamov et al. 2021). Khodachenko et al. (2019) confirmed the importance of Coriolis force, particularly for GJ 436b, and pointed out that the variations in stellar wind parameters could be the reason for the dispersion in  $\text{Ly}\alpha$  observation data. With a consistent photoevaporative planetary wind model that combined more realistic photochemical and thermodynamic processes, this work reached a qualitatively similar conclusion that  $\text{Ly}\alpha$  is

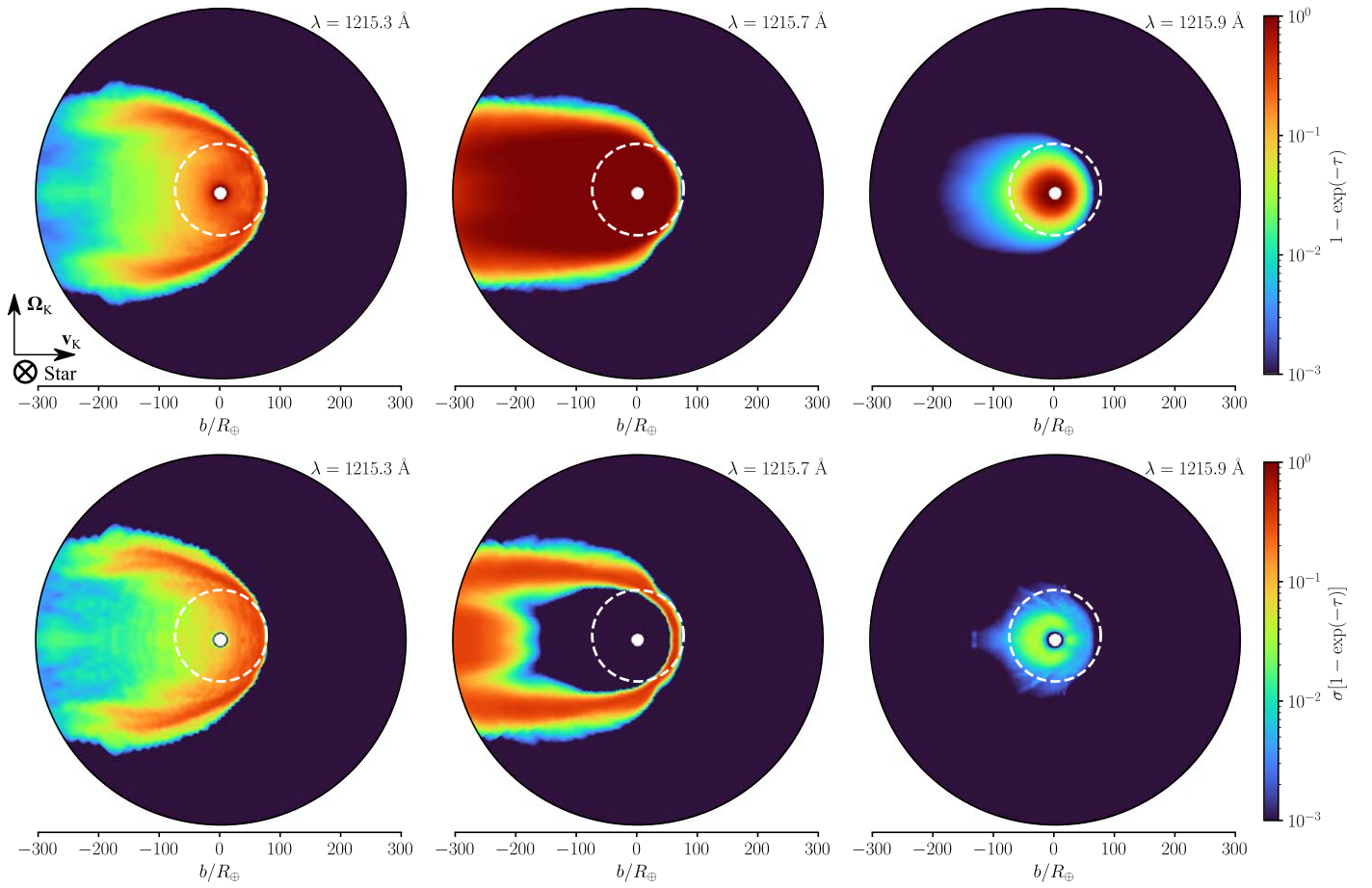


**Figure 11.** Similar to Figure 4, but for the wavelengths  $(\lambda/\text{\AA}) \in \{1215.3, 1215.7, 1215.9\}$  near the Ly $\alpha$  line.

more responsible of the contact surface, namely, the “envelope” of the comet-like tail that is susceptible to Coriolis force.

In order to portray the stellar–planetary wind interactions with higher completeness, Ly $\alpha$  alone seems insufficient. Villarreal D’Angelo et al. (2021) and Shaikhislamov et al. (2021) attempted to break the degeneracy of wind parameters by introducing H $\alpha$  or He\* in addition to Ly $\alpha$  in 3D simulations for GJ 436b. We have a similar philosophy implemented with significantly improved self-consistency in the thermochemistry of the relevant chemical species, and we find that He\*, which is sensitive to ionized photoevaporation, can be a particularly powerful probe complementing the information provided by the Ly $\alpha$  profile. Joint observation of He\* and Ly $\alpha$  line profiles, particularly multiple simultaneous transit observations, will be instrumental in helping us develop a comprehensive knowledge on the morphology and kinematics of atmospheric loss on different spatial scales. With adequate information on the host star SED or concrete measurements of the He\* line ratio (Section 5.3), we may be able to break the degeneracy in the He\* observation and also acquire more knowledge about the characteristics and variabilities of stellar wind from the host star. Hybrid models combining hydrodynamics with particles-based simulations are perhaps mandatory to fully characterize the various species of the outflow at highest altitude, especially neutral hydrogen.

## 6. Summary

This paper presents simulations of the metastable helium absorption lines in the transmission of WASP-107b. We

employ full 3D hydrodynamic simulations to model the dynamics of evaporating planetary atmospheres, in which nonequilibrium thermochemistry and ray-tracing radiative transfer are coevolved. The processes that populate and depopulate the metastable state of neutral helium are included in the thermochemical network and solved consistently. These allow us to predict the mass-loss rate, the temperature profile, and synthetic observations in both Ly $\alpha$  and He\*; we note that previous works often have to assume or prescribe the first two.

By exploring the parameter space, we find a plausible model for WASP-107b that also involves a stellar wind stronger than the solar wind. This model launches a photoevaporative outflow with a mass-loss rate of  $\dot{M} \simeq 1.0 \times 10^{-9} M_{\oplus} \text{ yr}^{-1}$ . The predicted He\* line profiles and light curves exhibit reasonable agreement with existing observations. The time-averaged transmission spectrum has a  $\sim 1:4 > 1:8$  line ratio, while the light curve holds a considerable asymmetry about the transit median. A comet-like tail trailing the planet is a natural explanation of these observations. We argue that such a tail is the result of a relatively strong stellar wind rather than radiation pressure, because (1) the low overall abundance of He\* and (2) the photon momenta deposited by absorption and scattering are quickly thermalized by collisional momentum relaxation. The incoming stellar wind triggers shear instabilities, and the He\* transit depth fluctuates by 5%–20% at a roughly  $\sim 0.2$ -day timescale consequently. Tuning the characteristics of stellar wind in a plausible range does affect the spectral line shapes through alternating the direction and configuration of the tail, yet the equivalent width is largely invariant. The Ly $\alpha$  transmission

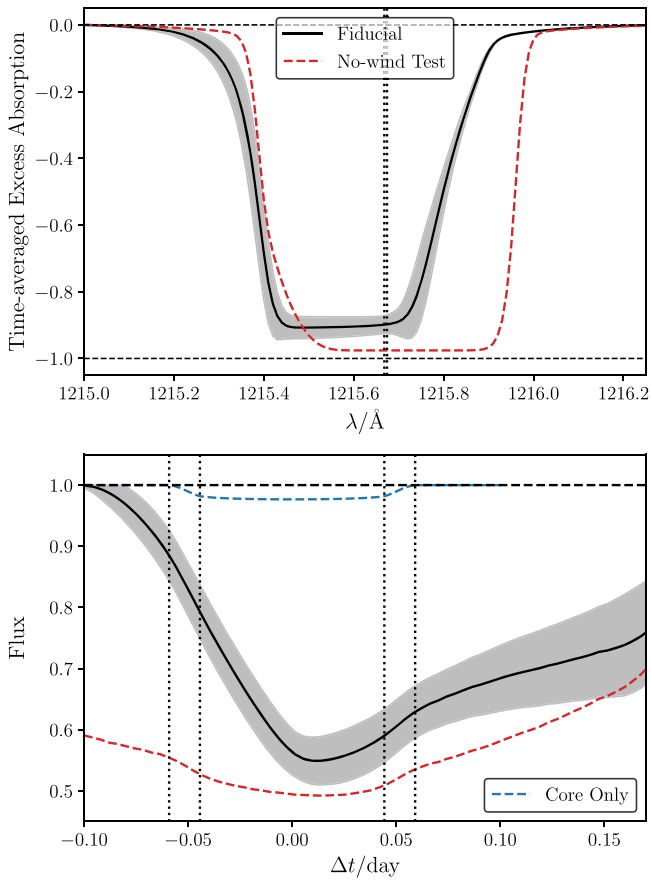


**Figure 12.** Similar to Figure 5, but for the Ly $\alpha$  synthetic spectra based on model 107-0 and its corresponding test models only. The wavelength window for the light curves is  $(\lambda/\text{\AA}) \in [1215.0, 1216.25]$ . Note that the time-averaged line profiles in the top panel have saturated shapes but the excess absorption amplitudes do not reach  $\langle \Delta\epsilon \rangle = -1$ , because (1) the extinction by the planet core is subtracted from the total absorption and (2) the full ingress of the Ly $\alpha$  absorption region is delayed by the stellar wind.

spectra and light curve synthesized using the fiducial model 107-0 suggest stronger light-curve asymmetry and variabilities due to shear instabilities. We propose that surveys of exoplanets in Ly $\alpha$  and He\* simultaneously are crucial for understanding planetary outflow and stellar wind.

Looking ahead, planetary outflow modulated by stellar winds may extract positive or negative orbital angular momentum from the planet via interactions with the circumstellar gas by dynamical (anti)friction (Li et al. 2020; Kurbatov & Bisikalo 2021) and may then lead to migrations of planetary orbits. Planetary magnetic fields and the fields carried by stellar winds or coronal ejecta may also play essential roles in shaping the dynamics of an evaporating close-in planet. Future simulations should have magnetohydrodynamics involved in these processes with improved consistency and will potentially shed light on the evolution of magnetic fields when compared to observations.

This work is supported by the Center for Computational Astrophysics of the Flatiron Institute and the Division of Geological and Planetary Sciences of the California Institute of Technology. L.W. acknowledges the computing resources provided by the Simons Foundation and the San Diego Supercomputer Center. We thank our colleagues (in alphabetical order) Philip Armitage, Zhuo Chen, Jeremy Goodman,

Xinyu Li, Mordecai Mac-Low, Songhu Wang, and Andrew Youdin, for helpful discussions and comments. We particularly thank the anonymous referee for the constructive comments and suggestions.

### ORCID iDs

Lile Wang  <https://orcid.org/0000-0002-6540-7042>

Fei Dai  <https://orcid.org/0000-0002-8958-0683>

### References

- Allart, R., Bourrier, V., Lovis, C., et al. 2018, *Sci*, **362**, 1384  
Allart, R., Bourrier, V., Lovis, C., et al. 2019, *A&A*, **623**, A58  
Anderson, D. R., Collier Cameron, A., Delrez, L., et al. 2017, *A&A*, **604**, A110  
Berrington, K. A., Burke, P. G., Freitas, L. C. G., & Kingston, A. E. 1985, *JPhB*, **18**, 4135  
Bourrier, V., Ehrenreich, D., & Lecavelier des Etangs, A. 2015, *A&A*, **582**, A65  
Bourrier, V., & Lecavelier des Etangs, A. 2013, *A&A*, **557**, A124  
Bourrier, V., Lecavelier des Etangs, A., & Dupuy, H. 2013, *A&A*, **551**, A63  
Bourrier, V., Lecavelier des Etangs, A., Tanaka, Y. A., & Vidotto, A. A. 2016, *A&A*, **591**, A121  
Carolan, S., Vidotto, A. A., Plavchan, P., Villarreal D'Angelo, C., & Hazra, G. 2020, *MNRAS*, **498**, L53  
Chachan, Y., Jontof-Hutter, D., Knutson, H. A., et al. 2020, *AJ*, **160**, 201  
Chauvin, G. 2018, arXiv:1810.02031  
Christie, D., Arras, P., & Li, Z.-Y. 2016, *ApJ*, **820**, 3  
Dai, F., & Winn, J. N. 2017, *AJ*, **153**, 205  
Debrecht, A., Carroll-Nellenback, J., Frank, A., et al. 2020, *MNRAS*, **493**, 1292  
Draine, B. T. 2011, *Physics of the Interstellar and Intergalactic Medium* (Princeton, NJ: Princeton Univ. Press)  
Draine, B. T., & Bertoldi, F. 1996, *ApJ*, **468**, 269  
Drake, G. W. 1971, *PhRvA*, **3**, 908  
Ehrenreich, D., Bourrier, V., Wheatley, P. J., et al. 2015, *Natur*, **522**, 459  
Esquivel, A., Schneider, M., Villarreal D'Angelo, C., Sgró, M. A., & Krapp, L. 2019, *MNRAS*, **487**, 5788  
France, K., Loyd, R. O. P., Youngblood, A., et al. 2016, *ApJ*, **820**, 89  
Gao, P., & Zhang, X. 2020, *ApJ*, **890**, 93  
Gudel, M. 1992, *A&A*, **264**, L31  
Heays, A. N., Bosman, A. D., & van Dishoeck, E. F. 2017, *A&A*, **602**, A105  
Holmström, M., Ekenbäck, A., Selsis, F., et al. 2008, *Natur*, **451**, 970  
Khodachenko, M. L., Shaikhislamov, I. F., Fossati, L., et al. 2021, *MNRAS Letters*, **503**, L23  
Khodachenko, M. L., Shaikhislamov, I. F., Lammer, H., et al. 2017, *ApJ*, **847**, 126  
Khodachenko, M. L., Shaikhislamov, I. F., Lammer, H., et al. 2019, *ApJ*, **885**, 67  
Khodachenko, M. L., Shaikhislamov, I. F., Lammer, H., & Prokopov, P. A. 2015, *ApJ*, **813**, 50  
Kirk, J., Alam, M. K., López-Morales, M., & Zeng, L. 2020, *AJ*, **159**, 115  
Kreidberg, L., Line, M. R., Thorngren, D., Morley, C. V., & Stevenson, K. B. 2018, *ApJL*, **858**, L6  
Kurbatov, E. P., & Bisikalo, D. V. 2021, arXiv:2101.04112  
Lavie, B., Ehrenreich, D., Bourrier, V., et al. 2017, *A&A*, **605**, L7  
Li, X., Chang, P., Levin, Y., Matzner, C. D., & Armitage, P. J. 2020, *MNRAS*, **494**, 2327  
Libby-Roberts, J. E., Berta-Thompson, Z. K., Désert, J.-M., et al. 2020, *AJ*, **159**, 57  
Lloyd, R. O. P., France, K., Youngblood, A., et al. 2016, *ApJ*, **824**, 102  
McCann, J., Murray-Clay, R. A., Kratter, K., & Krumholz, M. R. 2019, *ApJ*, **873**, 89  
McElroy, D., Walsh, C., Markwick, A. J., et al. 2013, *A&A*, **550**, A36  
Miguel, Y., Guillot, T., & Fayon, L. 2016, *A&A*, **596**, A114  
Ninan, J. P., Stefansson, G., Mahadevan, S., et al. 2020, *ApJ*, **894**, 97  
Norcross, D. W. 1971, *JPhB*, **4**, 652  
Nortmann, L., Pallé, E., Salz, M., et al. 2018, *Sci*, **362**, 1388  
Oklopčić, A. 2019, *ApJ*, **881**, 133  
Oklopčić, A., & Hirata, C. M. 2018, *ApJL*, **855**, L11  
Parker, E. N. 1958, *ApJ*, **128**, 664  
Piaulet, C., Benneke, B., Rubenzahl, R. A., et al. 2021, *AJ*, **161**, 70  
Rubenzahl, R. A., Dai, F., Howard, A. W., et al. 2021, *AJ*, **161**, 119  
Salz, M., Czesla, S., Schneider, P. C., et al. 2018, *A&A*, **620**, A97  
Seager, S., & Sasselov, D. D. 2000, *ApJ*, **537**, 916

- Shaikhislamov, I. F., Khodachenko, M. L., Lammer, H., et al. 2018, *ApJ*, **866**, 47
- Shaikhislamov, I. F., Khodachenko, M. L., Lammer, H., et al. 2021, *MNRAS*, **500**, 1404
- Spake, J. J., Sing, D. K., Evans, T. M., et al. 2018, *Natur*, **557**, 68
- Thomas, M. A., & Humberston, J. W. 1972, *JPhB*, **5**, L229
- Traub, W. A., & Oppenheimer, B. R. 2010, in *Exoplanets*, ed. S. Seager (Tucson, AZ: Univ. Arizona Press), 111
- Tremblin, P., & Chiang, E. 2013, *MNRAS*, **428**, 2565
- Turner, J. D., Christie, D., Arras, P., Johnson, R. E., & Schmidt, C. 2016, *MNRAS*, **458**, 3880
- Venzmer, M. S., & Bothmer, V. 2018, *A&A*, **611**, A36
- Villarreal D'Angelo, C., Vidotto, A. A., Esquivel, A., Hazra, G., & Youngblood, A. 2021, *MNRAS*, **501**, 4383
- Wang, L., & Dai, F. 2018, *ApJ*, **860**, 175
- Wang, L., & Dai, F. 2019, *ApJL*, **873**, L1
- Wang, L., & Dai, F. 2021, *ApJ*, 914, 98
- Wood, B. E., Redfield, S., Linsky, J. L., Müller, H.-R., & Zank, G. P. 2005, *ApJS*, **159**, 118
- Youngblood, A., France, K., Loyd, R. O. P., et al. 2016, *ApJ*, **824**, 101
- Youngblood, A., France, K., Loyd, R. O. P., et al. 2017, *ApJ*, **843**, 31
- Zhang, M., Knutson, H. A., Wang, L., et al. 2021, *AJ*, **161**, 181